Effect of different grade levels of calcined clays on fresh and hardened properties of ternary-blended cementitious materials for 3D printing

Chen, Yu; Romero Rodriguez, Claudia; Li, Zhenming; Chen, Boyu; Copuroglu, Oguzhan; Schlangen, Erik

DOI
10.1016/j.cemconcomp.2020.103708

Publication date
2020

Document Version
Final published version

Published in
Cement and Concrete Composites

Citation (APA)
Chen, Y., Romero Rodriguez, C., Li, Z., Chen, B., Copuroglu, O., & Schlangen, E. (2020). Effect of different grade levels of calcined clays on fresh and hardened properties of ternary-blended cementitious materials for 3D printing. *Cement and Concrete Composites*, *114*, Article 103708. https://doi.org/10.1016/j.cemconcomp.2020.103708

Cement and Concrete Composites 114 (2020) 103708

Contents lists available at ScienceDirect

Cement and Concrete Composites

journal homepage: http://www.elsevier.com/locate/cemconcomp

Effect of different grade levels of calcined clays on fresh and hardened properties of ternary-blended cementitious materials for 3D printing

Yu Chen *, Claudia Romero Rodriguez, Zhenming Li, Boyu Chen, Oğuzhan Çopuroğlu, Erik Schlangen

Microlab, Faculty of Civil Engineering and Geosciences, Delft University of Technology, Delft, the Netherlands

ARTICLE INFO

Keywords:
3D concrete printing
Sustainability
Compressive strength
Hydration kinetics
Ternary-blended cementitious materials
Calcined clay

ABSTRACT

This study aims to investigate the influences of different grades of calcined clay on 3D printability, compressive strength (7 days), and hydration of limestone and calcined clay-based cementitious materials. Calcined clays that contained various amounts of metakaolin were achieved by blending low-grade calcined clay (LGCC) and high-grade calcined clay (HGCC) in three different proportions. The results revealed that increasing the HGCC% ranging from 0 wt% to 50 wt% in calcined clay could: (1) increase the flow consistency; (2) impressively improve the buildability, and reduce the printability window of the fresh mixtures; (3) enhance and accelerate the cement hydration. However, increasing HGCC% led to an increase of air void content in the interface region of the printed sample, which weakened the compressive strength of the printed sample at 7 days. Besides, it confirmed that the cold-joint/weak interface was easily formed by using the fresh mixture with a high structuration rate.

1. Introduction

Over the years, 3D concrete printing (3DCP), also known as additive manufacturing of concrete, has received considerable attention from both academia and industry [1–6] due to numerous benefits for concrete construction, through eliminating formwork, optimizing material use, enhancing the freedom of building design, reducing wastes, labors and costs [7–10]. Two main techniques of 3DCP, i.e., particle bed- and extrusion-based approaches, are currently available [5,11]. Over half of the investigations focus on the employment of extrusion-based 3DCP [11]. Compared with the particle bed technique, the extrusion-based approach seems to be more appropriate for large-scale and in-situ construction [12].

The development of 3D printable mixtures might be one of the most critical aspects in the field of extrusion-based 3DCP. The fresh mixture should exhibit noticeable thixotropic behavior in the 3DCP process, i.e., high fluidibility and low viscosity for extrusion, as well as high shape stability and structuration rate after layer deposition, which is regarded as the main challenge in the material development aspect [13–15]. Extrudability, flowability, open time (also referred to as printability window [16]), buildability, and layer adhesiveness were summarized as the main criteria for a cementitious material to be 3D printable by [17,18]. Among them, extrudability, printability window, and buildability can be recognized as the primary features of the 3D printability.

Extrudability is used to describe the ease of extruding a mixture through a nozzle continuously at a given printing speed [5]. The extrudability of one mixture relies on its rheological behaviors, namely, static yield stress and plastic viscosity, which are usually characterized by using a shear-based rheometer (with a specific protocol) and Bingham model (see [19–21]). Nonetheless, in many cases, the unreliability of the results can not be avoided due to the wall slip and plug flow of highly concentrated mixture during the test [22,23]. According to [4,23–26], ram extruder could also be used to characterize the flow properties of high stiffness fresh mixtures for which a shear-based rheometer would not be valid. The advantages of using a ram extrusion test become significant for investigating the rheology of fiber-reinforced cementitious materials [23]. As illustrated by Chen et al. [4], it is feasible to quantify the rheological parameters of printable cementitious materials, such as flow consistency, and elongational yield stress, by employing a specific ram extrusion test and Basterfield et al. [27] model. Printability window and buildability, as two main subjects constrained by the 3D printing setup, rely mainly on the thixotropic behavior of the fresh mixtures. Printability window is defined as the timespan during which a mixture could be printed via a nozzle with the

---

* Corresponding author.

E-mail addresses: Y.Chen-6@tudelft.nl (Y. Chen), C.RomeroRodriguez@tudelft.nl (C. Romero Rodriguez), Z.Li-2@tudelft.nl (Z. Li), B.Chen-4@tudelft.nl (B. Chen), O.Copuroglu@tudelft.nl (O. Çopuroğlu), Erik.Schlangen@tudelft.nl (E. Schlangen).

https://doi.org/10.1016/j.cemconcomp.2020.103708
Received 18 March 2020; Received in revised form 25 May 2020; Accepted 8 June 2020
Available online 4 July 2020

acceptable printing quality [16]. It is a crucial parameter to evaluate the extrudability loss of one mixture with time. Due to the absence of formwork, the extruded cementitious materials are required to sustain its geometry under the loading from the upper layers, which is referred to as the term of buildability [9,12,14,28]. The test protocols of printability window and buildability have been developed and performed by past works (see [12,16,28–31]).

To date, considerable studies have been conducted for developing 3D printable mixtures. Instead of plain cement, blended cement is used in most of the 3D printable cementitious materials. Supplementary cementitious materials (SCMs), e.g., limestone, fly ash, silica fume, and slag, have been utilized as an ingredient of the binder in 3D printable cementitious materials [8,9]. Nerella et al. [5] proposed a printable mixture containing 55 wt% of Portland cement (PC), 30 wt% of fly ash, and 15 wt% of micro silica (silica fume). Panda et al. [13] used nano-attapulgite clay as an additive to improve the buildability and mechanical performance of a printable cementitious material with 70 wt % of fly ash in the binder. Chaves Figueiredo et al. [23] developed a fiber-reinforced printable cementitious composite that consists of 35 wt % blast furnace slag, 50 wt% limestone, and 15 wt% PC. Using blended cement could be regarded as a sustainable approach in 3DCP due to the reduction of PC consumption [8].

However, these SCMs, including slag, silica fume, and fly ash, are gradually being depleted [32]. For longer-term development, calcined clay appears to be a suitable alternative to SCMs, as suggested by [32, 33]. Remarkable benefits, i.e., low CO_2 footprint [32,34], abundant raw materials [35], good compressive strength [36,37], and capillary porosity refinement by pozzolanic reactions [35,38,39], could be achieved by using limestone calcined clay cement (LC3). The reactivity of calcined clay depends on the formation of metakaolin (MK) during the calcination of kaolinite clay at a temperature between 700 and 850 °C [39–41]. In contrast to using high-purity MK, calcined low-grade kaolinite clay (low MK content) shows a tremendous economic advantage as a clinker substitute [32,39,41]. Also, calcined clay may be an ideal ingredient for improving the 3D printability of cementitious materials. Tregger et al. [42] found that blending a certain amount of calcined clay (purified calcined kaolinite) in the paste could enhance the shape stability and green strength of the fresh mixture in comparison with using the same volume of fly ash. Recently, Muzenda et al. [43] reported that calcined clay could contribute to increase the thixotropic index, apparent viscosity, cohesion, static and dynamic yield stresses of the fresh LC3 paste.

Calcined clays that are sourced from different suppliers may exhibit different chemical compositions (especially MK contents and secondary phases), and physical properties, i.e., fineness, morphology, specific surface area, and density [33,44]. Those differences, which may be induced by the type of raw clays (1:1 or 2:1 clay), the heat treatment conditions, the temperature range of calcination and the purity of clay sources [45–47], may bring substantial influences on the fresh and hardened properties of cementitious materials. The term of different-grade was used in this paper to represent those differences in calcined clays.

The evidence from past work has demonstrated that the rheology and thixotropy of fresh mixtures can be modified by using different grades of calcined clay. Beigh et al. [48] studied the rheological behaviors of LC3 paste by using two different calcined clays. The authors found that the addition of different calcined clays could increase the structuration rate of the fresh mixture at rest in varying degrees to compare with plain cement paste, which may depend on the presence of uncalcined kaolinite clay. According to Chen et al. [44], increasing the MK content in calcined clay could shorten the initial setting time, and increase the extrusion pressure as well as the green strength of a developed limestone and calcined clay-based cementitious material at a very early age. Aramburo et al. [49] mentioned that the effects of different calcined clays on rheological behaviors of fresh pastes might be attributed to the reactivity of the added calcined clay, i.e., reactive aluminate content provided by MK. They observed that the increase of reactive aluminate content in calcined clay resulted in an enhancement of structural build-up behavior of the fresh paste.

On the other hand, in the context of mold-cast concrete, MK content (calcined kaolinite clay content) was believed to be the main parameter to influence the hardened properties of LC3 [39]. For LC3-50 blends (Clinker: 50 wt%; Limestone: 15 wt%; Calcined clay: 30 wt%; Gypsum: 5 wt%), the compressive strength from 1 day to 90 days can be enhanced with the increase of the calcined kaolinite clay content (MK content) [33]. Also, the clinker hydration is influenced by MK content. Zhao et al. [41] pointed out that MK accelerates the early-age hydration of clinker via the filler effect and subsequently reacts with calcium hydroxide to form calcium-aluminosilicate-hydrate (C-A-S-H). According to Avet et al. [39], for the LC3-50 systems containing calcined clay with more than 65% of MK, clinker hydration is surprisingly retarded after 3 days. This is probably due to a lack of pores above the critical size for the precipitation of hydrates.

To our knowledge, research on the development of limestone and calcined clay-based cementitious materials for extrusion-based 3DCP is still at an early stage. Few attempts have been made to explore the 3D printability of such ternary-blended cementitious materials by using different grades of calcined clay. Herein, the objective of this paper is to investigate the effects of different grades of calcined clay on the 3D printability, on the compressive strength, and on the hydration kinetics of such ternary-blended cementitious materials in the context of extrusion-based 3DCP. This study was organized into three distinct aspects, the first of which deals with the characterization of 3D printability. A specific ram extrusion test and Basterfield et al. model were initially utilized to quantify the extrusion rheology of fresh mixtures. After that, based on a lab-scale 3DCP setup, printability window and buildability were evaluated. Second, the compressive strength was measured on both mold-cast and printed samples at the material age of 7 days. Additionally, the air void content and distribution of printed samples were quantified by using 3D X-ray computed tomography scanning and image analysis. Third, isothermal calorimetry and thermogravimetric analysis were carried out for assessing phase assemblages of the resulting materials.

2. Material and methods

2.1. Raw materials and mix design

CEM I 52.5R type Portland cement (PC), limestone powder (LP), and calcined clay (CC) formed the binder of printable mixtures. Two types of calcined clay were used in this work. A low-grade calcined clay (LGCC), which contained about 50% of MK, was purchased from Argeco, France. The other one, with nearly 95% of MK, was regarded as a high-grade calcined clay (HGCC) supplied by Burgess, USA. Table 1 illustrates

Table 1
Physical characteristics and oxide composition from XRF of dry components in binders.

	PC	LP	LGCC	HGCC
Density [g/cm^3]	3.120	2.646	2.512	2.134
SSA [m^2/g]	1.16	1.22	10.06	12.60
D_{v50} [μm]	14.86	24.19	69.35	3.75
XRF [wt.%]				
CaO	68.7	39.6	0.6	0
SiO_2	17.4	0.2	55.1	47.3
Al_2O_3	4.1	0	38.4	50.6
Fe_2O_3	2.8	0.1	2.6	0.5
K_2O	0.6	0	0.2	0.2
TiO_2	0.3	0	1.1	1.3
ZrO_2	0	0	0.1	0
Other	6.1	60.1	1.9	0.1
Total	100.0	100.0	100.0	100.0

physical and X-ray fluorescence (XRF) characteristics of PC, LP, LGCC, and HGCC. The Brunauer-Emmett-Telle (BET) specific surface area (SSA) of all dry components was measured via the liquid nitrogen (N_2) adsorption method.

XRD was conducted through a PhilipsPW1830 powder X-ray diffractometer, with CuKα radiation operated at 45 kV and 40 mA, for 2θ values between 5° and 75°. The results for LGCC and HGCC, reported in Fig. 1, showed higher amorphous content in HGCC from the presence of a broad hump in the 2θ range of 15°–30° when compared to LGCC where it ranges from 20° to 28°. Besides, more crystalline phases, such as quartz (SiO_2), mullite ($3Al_2O_3{\cdot}2SiO_2$) and kaolinite ($Al_2O_3{\cdot}2SiO_2{\cdot}2H_2O$), were observed in LGCC. The chemical dissolution method, according to NEN-EN 196-2 [50], was used to quantify the reactive content of calcined clay. The results, in Table 2, showed that the reactive content of LGCC and HGCC was 48.8% and 75.1%, respectively. Due to the size limitation of the printing setup, the sand with the maximum grain size of 2 mm used as aggregate of the studied mixtures. The gradings of all dry components were presented in Fig. 2. HGCC was the finest powder with an average particle size (D_{v50}) of 3.75 μm. The morphological properties of LGCC and HGCC were reported in Fig. 3. For both LGCC and HGCC, the thin layered, irregular flaky morphology was observed.

Table 3 shows the specific proportions of the different mixtures studied in this paper. For all mixtures, PC was about 40% of the total binder mass. The limestone-to-calcined clay mass ratio of 1:2, which showed good early-age mechanical performance [38,44], was used in this research. Calcite from limestone could react with alumina species in pore solution to form hemi-/mono-carboaluminate, which in turn refilled the pores and stabilized the ettringite, resulting in a reduction in the porosity and an increase in the compressive strength [47,51]. In addition to mixture LCC, another two mixtures were prepared by replacing 25 wt% and 50 wt% of LGCC with HGCC to simulate the calcined clay with about 61.3 wt% and 72.5 wt% of MK, respectively. Mixture REF containing 0 wt% of calcined clay was used as a reference to investigate the effects of calcined clay on cement hydration and compressive strength of mold-cast samples. The sand-to-binder ratio and water-to-binder ratio was selected as 1.5 and 0.3, respectively. Besides, 2 wt.% of polycarboxylate ether (PCE)-based superplasticizer and 0.24 wt.% of methylcellulose-based viscosity modifying admixture (by weight of binder) were added to adjust the fresh state behaviors to satisfy the requirements for 3D printability based on our previous study [14]. The fresh mixtures were prepared by following a specific mixing protocol, as shown in Fig. 4. The time zero (T = 0 min) in this study was defined as the time of mixing liquid suspension (water + superplasticizer) with dry materials.

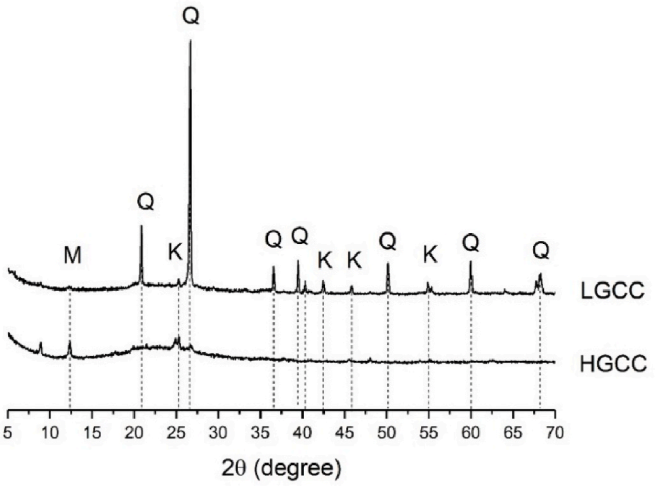

Fig. 1. XRD patterns of LGCC and HGCC. Q-quartz (SiO_2), M-mullite ($3Al_2O_3{\cdot}2SiO_2$), and K-kaolinite ($Al_2O_3{\cdot}2SiO_2{\cdot}2H_2O$).

Table 2
Reactive content of two different calcined clays (LGCC and HGCC).

	Total reactive content [wt.%]	Reactive silicate [wt.%]	Reactive aluminate [wt.%]	Other reactive content [wt.%]
LGCC	48.8	12.3	32.0	4.5
HGCC	75.1	34.6	39.9	0.6

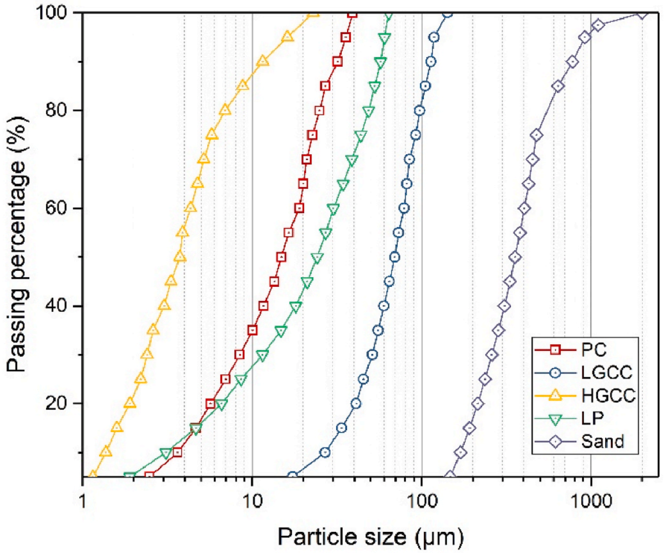

Fig. 2. The particle size distribution of PC, LGCC, HGCC, LP, and sand. The grain size of sand was measured by using a sieving machine. All other dry components were determined by laser diffractometry.

The influence of filler additions (limestone and calcined clay) on the total SSA of solid (SSA_{total}) of the binder system is calculated through:

$$SSA_{total} = \frac{M_{cem}SSA_{cem} + M_{filler}SSA_{filler}}{M_{cem} + M_{filler}} \tag{1}$$

where M_{cem} and M_{filler} are the mass percentages of PC and other fillers (LP, LGCC, HGCC) in the binder. SSA_{cem} and SSA_{filler} mean the specific surface areas of PC and other fillers (LP, LGCC, HGCC) in the binder. Table 4 presents the SSA_{total} results of different binders in this paper.

2.2. *Test procedures*

2.2.1. *Ram extrusion test*

A ram extruder (see Fig. 5(a)), which consisted of a barrel, a piston, a stand, and an orifice, was assembled in a servo-hydraulic Instron machine. The piston was connected to a 10 kN load cell that could measure the total extrusion force. Before the test, the barrel was filled with the fresh mixture. Care was taken to ensure a minimum content of entrapped air during the barrel filling process. Afterwards, the piston was operated with different speeds to extrude the fresh mixture through the orifice. All mixtures were tested at a material age of 15 ± 2 min. A typical trial of the ram extrusion test is shown in Fig. 5(c). The pre-test consists of a piston displacement from 0 to 29.5 mm. Two speeds (1 mm/s and 2 mm/s) were used in the pre-test stage. Within the piston displacement between 29.5 mm and 43 mm, 12 different piston speeds (V_0) were employed (for each test, only one speed was used), and the material flow rates (V) at the orifice were calculated by:

$$V = \frac{D_0^2}{D^2}V_0 \tag{2}$$

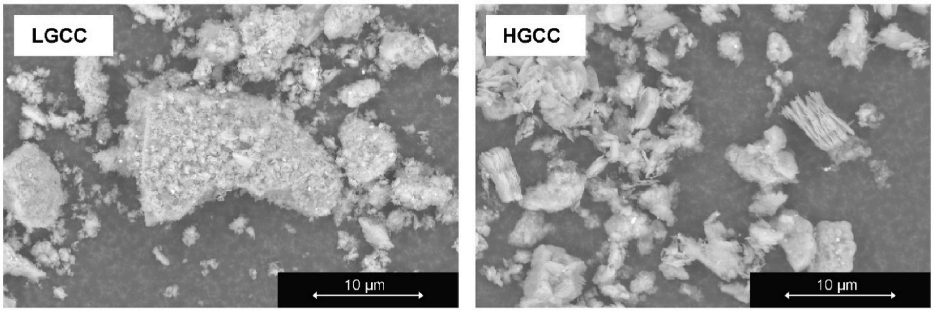

Fig. 3. Electron micrographs (secondary electron mode) of LGCC (left) and HGCC (right).

Table 3
Mix designs of cementitious materials prepared in this study.

Mixture	Mix Proportion							
	Binder [wt.%]				Sand and Water mass ratios		Admixture mass ratio	
	PC	LGCC	HGCC	LP	Sand/Binder	Water/Binder	SP/Binder	VMA/Binder
REF[a]	40	0	0	60	1.5	0.3	0.02	0.0024
LCC	40	40	0	20	1.5	0.3	0.02	0.0024
MCC	40	30	10	20	1.5	0.3	0.02	0.0024
HCC	40	20	20	20	1.5	0.3	0.02	0.0024

[a] REF was not developed for 3D printing. It was the reference for illustrating the effect of calcined clay on compressive strength (mold-cast samples) and hydration.

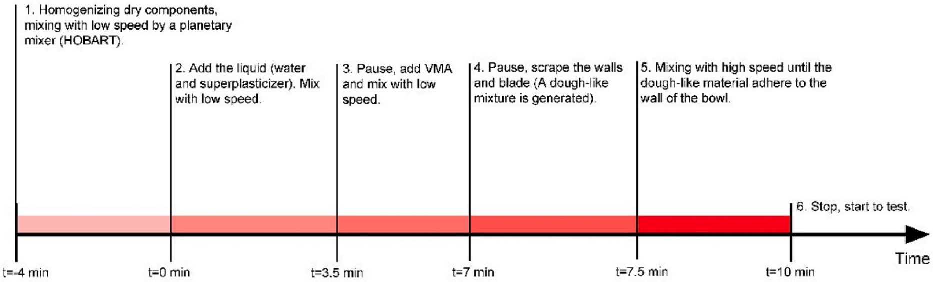

Fig. 4. Illustration of mixing procedures for the fresh mixture preparation.

Table 4
SSA_{total} of different binders.

	REF	LCC	MCC	HCC
SSA_{total} [m^2/g]	1.196	4.732	4.986	5.240

where D_0 and D represent the diameter of the barrel and die, respectively. The computed results were presented in Table 5. More test details and explanations could be found in Refs. [4]. Based on the collected extrusion forces, the upstream extrusion pressures were determined through:

$$P = \frac{4F}{\pi D_0^2} \tag{3}$$

where P and F stand for the extrusion pressure and the extrusion force, respectively, under one predefined piston speed.

The analytical relationship between the material flow rates and ram extrusion pressure at the orifice was given by Basterfield et al. [27]:

$$P = 2\sigma_0 \ln\frac{D_0}{D} + \frac{2}{3n}k(\sin\theta_{max}(1+\cos\theta_{max}))^n\left(1-\left(\frac{D}{D_0}\right)^{3n}\right)\left(\frac{2V}{D}\right)^n \tag{4}$$

where P is the extrusion pressure; V is the material flow speed at the orifice; σ_0 is the elongational yield stress; k is the flow consistency; n is the flow index; $\theta_{\max}$ is the maximum convergent flow angle (Fig. 5(b)). As suggested by Ref. [26,27], 45 was selected as the value of $\theta_{\max}$. Since the fresh cementitious materials also followed the Von–Mises criterion [25], the shear yield stress could be obtained by:

$$\tau_0 = \frac{\sigma_0}{\sqrt{3}} \tag{5}$$

where τ_0 means the shear yield stress.

2.2.2. 3D printing test

A lab-scale 3DCP setup at Delft University of Technology (TU Delft), as introduced in Ref. [14] was used for concrete printing. The 3DCP setup comprised two main components: a three-degree freedom Computer Numerical Control (CNC) machine and a PFT Swing-M type conveying pump (Fig. 6). The fresh mixture was prepared with a planetary mixing machine (HOBART) and then poured into the hopper (maximum volume: 38L) of the pump manually. A hose with a length of 5 m (Ø 25 mm) is connected to the pump and a printhead/nozzle. The latter is mounted on the z-axis arm of the CNC machine. The moving speed of the nozzle was adjusted between 35 mm/s and 100 mm/s. As shown in Fig. 7, two types of nozzles were used in this study. Nozzle 1 is based on a hybrid back- and down-flow extrusion mechanism. It consists of a rectangle opening with dimensions of 40x13.5 mm^2. Nozzle 2

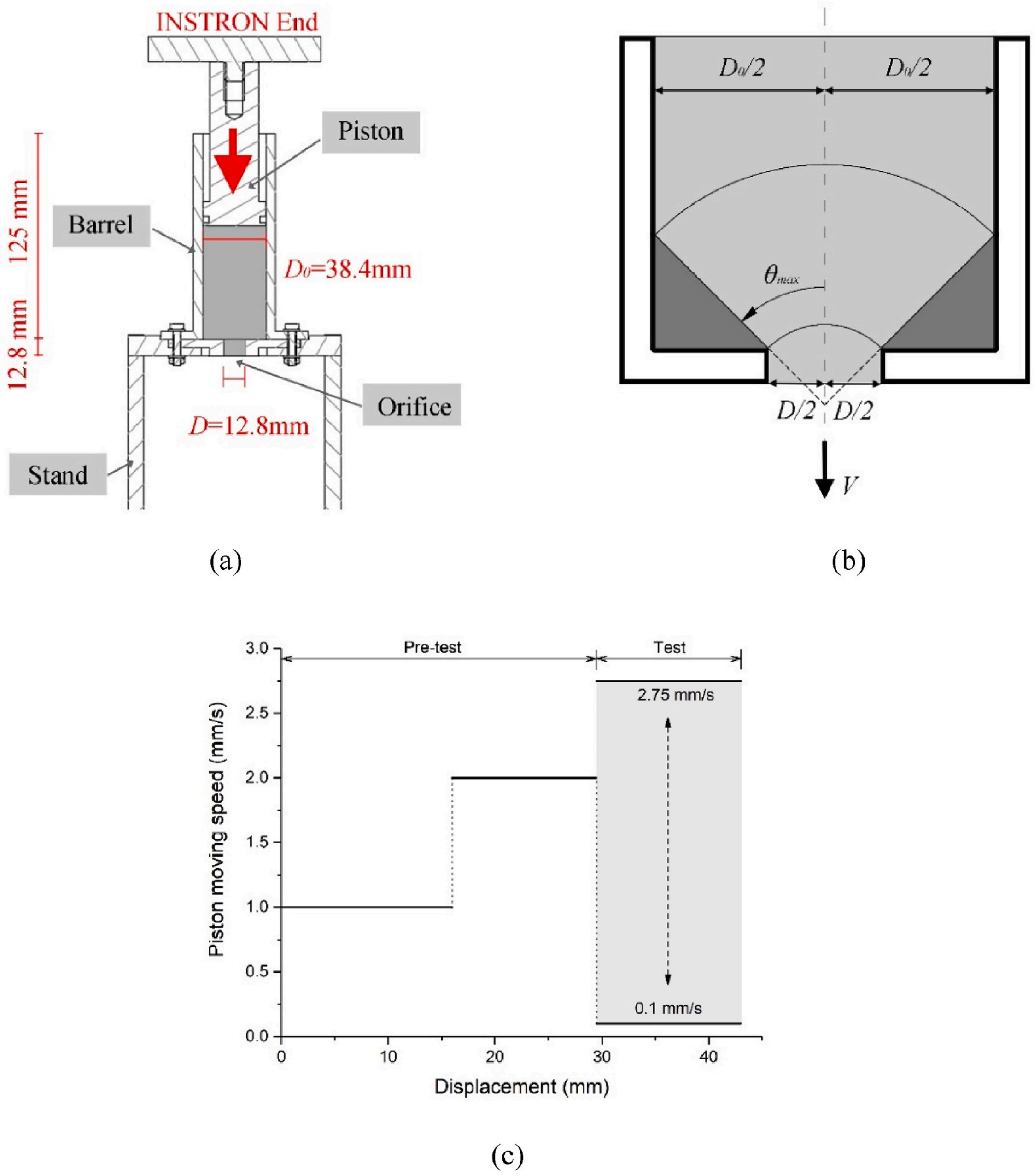

Fig. 5. (a) Schematic drawing of the ram extruder; (b) Diagram of the orifice entrance flow region in a spherical coordinate system, according to Ref. [26,27]; (c) A typical trial of the ram extrusion test - predefined piston moving speed vs. displacement.

(down-flow) contains a round opening with a diameter of 15 mm. Printing works, and other tests in this study were performed under the room temperature of 20 ± 2 °C and at around 55% RH.

Table 5
Piston speed (V_0) and computed material flow rate (V) at the orifice.

V_0 [mm/s]	V [mm/s]
0.10	0.90
0.25	2.25
0.50	4.50
0.75	6.75
1.00	9.00
1.25	11.25
1.50	13.50
1.75	15.75
2.00	18.00
2.25	20.25
2.50	22.50
2.75	24.75

2.2.2.1. Printability window. The test was performed as follow:

- First, 12L of the fresh mixture was prepared and poured into the hopper of the printer.
- After 10 min (material age: 20 min), the test is started. By using nozzle 1, one filament (with a designed dimension of 800 mm in length, 40 mm in width, and 13.5 mm in height) was extruded at a printing speed of 47 mm/s (material flow rate: 1.5 L/min). Every 10 min, a new filament was printed. During the 10 min time gap between the start of mixture preparation and the test, a pre-pumping session of 5 min was arranged.

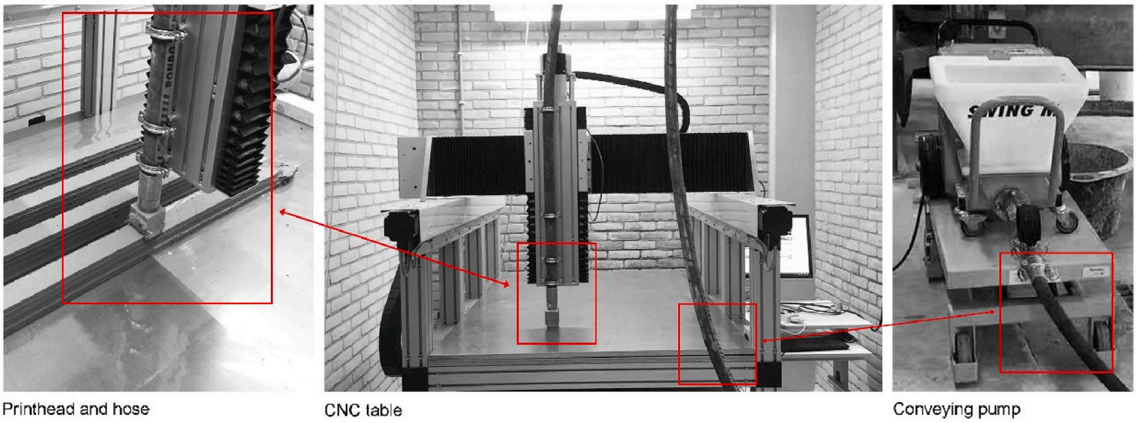

Fig. 6. A lab-scale 3DCP setup at TU Delft. It consists of a CNC table, a conveying pump, a material hose, and a printhead (nozzle).

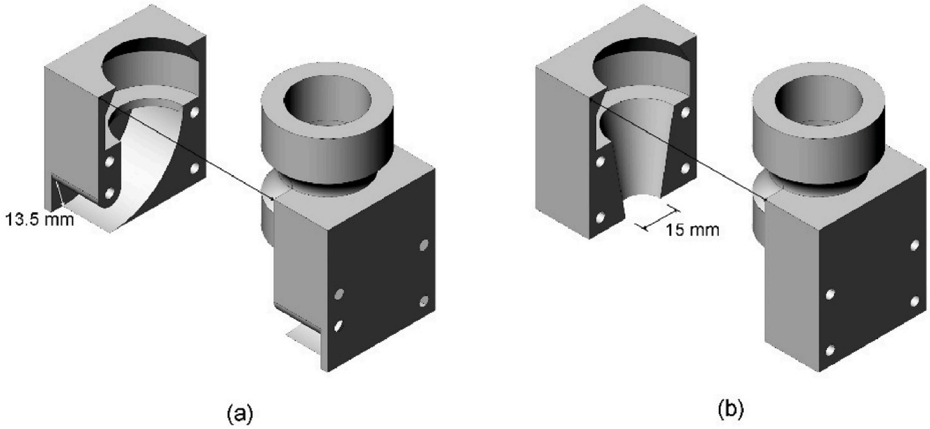

Fig. 7. (a) Nozzle 1 with a rectangle opening (40 × 13.5 mm^2); (b) Nozzle 2 with a round opening (Ø 15 mm).

- Third, the width of the extruded filament was measured at 6 different positions. The whole test was terminated once the disruption of filament occurred, or the average width of extruded filament was smaller than 35 mm.

2.2.2.2. Buildability. Two methods were employed to evaluate the buildability of the different mixtures. The test parameters of both methods were summarized in Table 6. Method 1 is quite similar to the buildability test that was proposed by Nerella et al. [12]. The test started at the material age of 20 min. A wall was designed to stack 21 layers. Nozzle 1 was employed for method 1. For each layer, there was only one filament (designed dimension: 900 mm length, 40 mm width, and 13.5 mm height). The process of method 1 is schematized in Fig. 8(a). The fresh mixture was deposited from position A to B at a constant printing speed of 47 mm/s. Once the nozzle reached position B (one filament was finished), the printing work was paused. The nozzle was programmed to be lifted at a maximum height of 285 mm and then to move to Position A. The time gap between two layers was set as 30s. Method 2 employed nozzle 2 to print a designed object with a non-stop printing process (Fig. 8(b)). The path length of each layer was 4200 mm. The height of the nozzle was increased to 8.5 mm each time at the start position C. The time interval between two subsequent layers was 57s. In comparison to method 1, a faster printing speed (75 mm/s) was utilized in method 2. During the test process (both methods 1 and 2), the height of the printed object was measured and recorded continuously. The test may be terminated earlier (before finishing the printing work) due to collapse by buckling.

Table 6
Printing parameters for buildability test.

	Method 1	Method 2
Nozzle type	Nozzle 1	Nozzle 2
Nozzle opening [mm]	40x13.5	Ø 15
Layer thickness [mm]	13.5	8.5
Nozzle moving speed [mm/s]	47	75
Path length for each layer [mm]	900	4200
Material flow rate [L/min]	1.5	0.9
Time interval [s]	30	57
Designed layer number	21	18
Designed structure height [mm]	283.5	153
Test start time [material age: min]	20	20

2.2.3. Compressive strength test

Printed prisms that contained 4 stacked layers (Length: 800 mm; Width: 42–44 mm; Height: 50–54 mm) were manufactured using the 3DCP setup (nozzle 1). The nozzle moving speed and the material flow rate were fixed at 35 mm/s and 1.2 L/min, respectively. The time interval between two adjacent layers was 2 min. Note that, the fresh mixtures in this study showed low slump during layer deposition. Thus, the printed filament was wider than the nozzle opening (40 mm). 40 mm cube specimens were sawn from the 3D printed prisms before performing the test. As illustrated by Ref. [52,53], the anisotropic properties of 3D printed concrete should be considered. Thus, the compressive strength of printed samples was tested along with three loading directions: D1, D2, and D3 (see Fig. 9). For each mixture and each direction, three samples were prepared and tested. Besides, to determine the influence of the printing process on compressive strength, 40x40x40

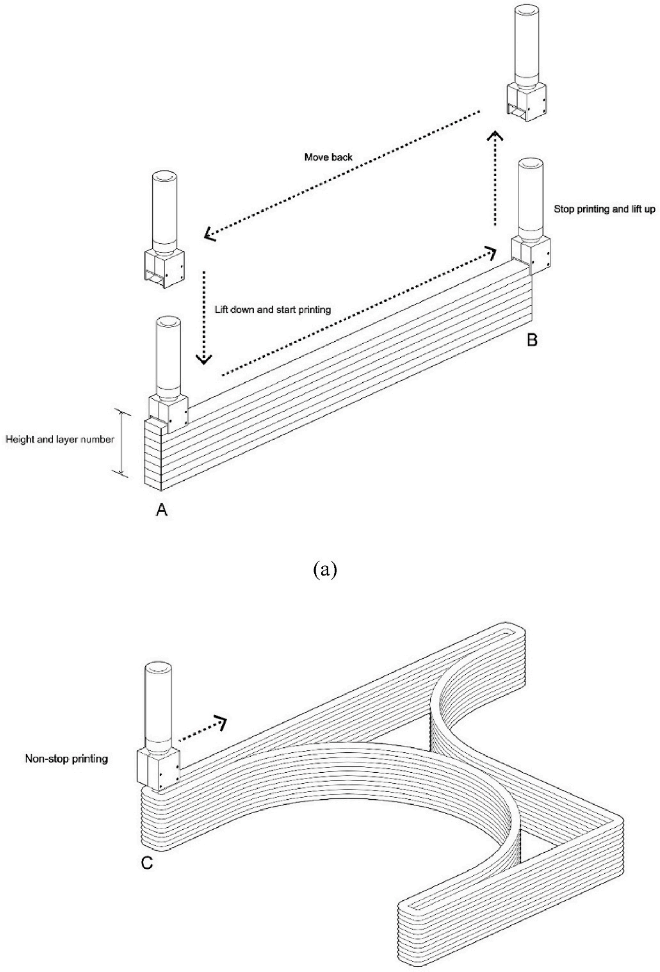

(a)

(b)

Fig. 8. Schematic diagram of buildability test: (a) Method 1 (by using nozzle 1); (b) Method 2 (by using nozzle 2).

mm^3 mold-cast specimens were also prepared. Before the test, all samples were cured and stored in a fog room (20 ± 2 °C and above 95% RH). The compressive strength test was conducted under a loading rate of 2.4 kN/s according to the specifications of NEN-EN 196-1 [54] at a material age of 7 days.

2.2.4. *Air void analysis*

The air void content and distribution of printed specimens were determined using 3D X-ray computed tomography (CT) scanning and image analysis through the open-source software ImageJ. Cylindrical samples (25 mm diameter and 24 mm height) were drilled and sawn from the upmost two layers of 3D printed beams, manufactured in Section 2.2.3. The prepared sample was scanned with a Phoenix Nanotom Micro CT-Scanner. The obtained resolution was 13.3 μm per voxel. Reconstruction of the projections into a 3D volume was conducted via the dedicated Phoenix Datos|x software. A cylindrical region of interest (ROI), as shown in Fig. 10(a), was extracted from the image stack to perform the subsequent image analysis. Employing the Trainable Weka Segmentation (TWS) plugin from ImageJ [55,56], the voids from each image were segmented (Fig. 10(b)). Afterwards, the void content and average void diameter were computed through the function Analyze Particles in ImageJ.

2.2.5. *Isothermal calorimetry test*

An eight-channel TAM Air isothermal calorimeter was used to measure the heat released during the first 7 days (168h) of hydration. The test procedures were the same as described by Chen et al. [14]. All paste mixtures were prepared according to the mixing procedure in Fig. 4. A 20 ml glass vessel was filled with 6g of paste. The vessel was sealed and moved into the calorimeter under the temperature of 20 °C. Heat values were collected after every 20s.

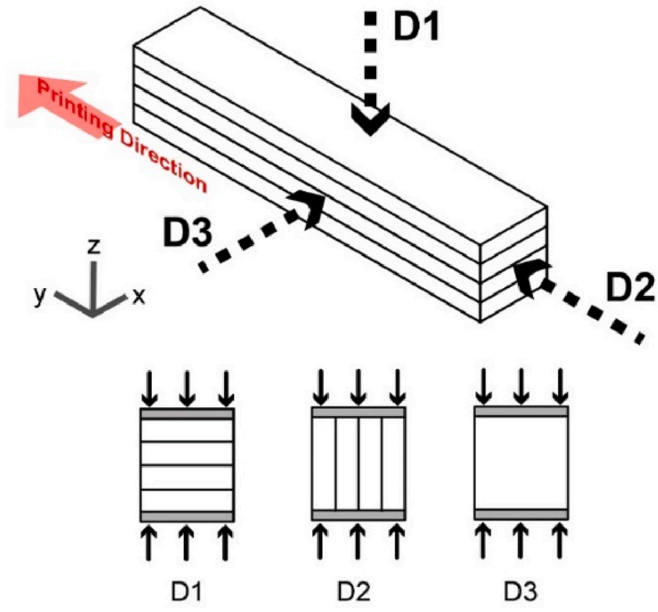

Fig. 9. Schematic view of the three testing directions for conducting the compressive strength test. D1 - loading on z-direction; D2 - loading on y-direction; D3 - loading on x-direction.

2.2.6. *Thermogravimetric analysis*

The paste mixtures from Section 2.2.5. were also used for the thermogravimetric analysis (TGA). The cast cylindrical specimens (33.5 mm diameter and 67.5 mm height) were stored at the fog room with the curing conditions (20 ± 2 °C, above 99% RH) up to the time of testing. A three-step procedure, as described by Lothenbach et al. [57], was used for powder sample preparation:

- First, crushing and grinding the sample in isopropanol solvent for about 10–15 min;
- Second, filtrating the suspension by using a Büchner funnel and an aspirator pump (the size of filter paper was 8 μm), followed by washing the solid with diethylene ether to remove the isopropanol;
- Third, drying the powder for about 8 min in a 40 °C aerated oven. The samples were stored in a light vacuum desiccator and tested within 3 days.

TGA was employed to quantify the hydrate water (H) and calcium hydroxide (CH) of different mixtures at the ages of 1, 2, 3, and 7 days. Netzsch STA 449 F3 Jupiter was utilized for the test. For each mixture, about 50 mg of paste sample that was placed in an alumina crucible was heated from 40 to 900 °C with a heating rate of 10 °C/min and under an argon environment with a flow rate of 30 ml/min.

3. Results

3.1. *Ram extrusion rheology*

Fig. 11(a) presents an example of the extrusion force concerning piston displacement. A pre-test zone (displacement: 0–29.5 mm) was utilized to compact the fresh mixture and transfer the material status from a static state to a dynamic state, which has been explained in

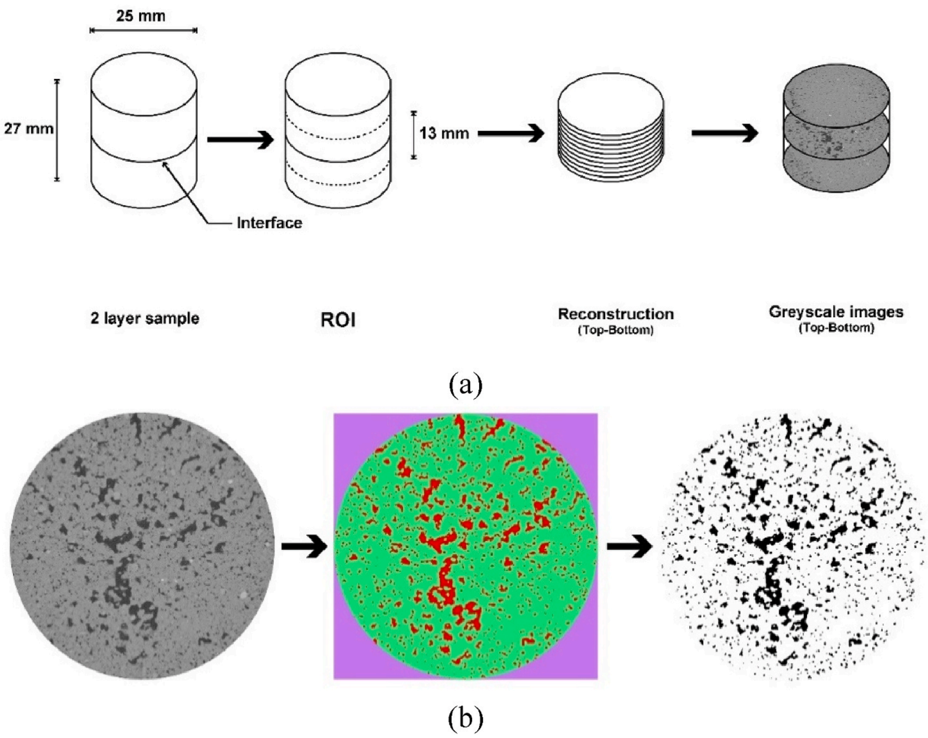

Fig. 10. (a) Illustration of sample preparation and CT scanning; (b) A typical example of the greyscale image segmentation process for determining the void area via TWS (ImageJ).

Ref. [4]. It could be noticed that the piston started to touch the fresh mixture at a displacement of about 11 mm. During the displacement from 11 mm to 16 mm (piston speed: 1 mm/s), an unstable curve pattern was observed due to the existence of air bubbles and the thixotropy of the fresh mixture. The curve becomes relatively stable at the end of the pre-test zone under the piston speed of 2 mm/s. Afterwards, the piston was driven under a predefined speed (see Table 5). Relatively flat curves could be found in the test zone. The average upstream extrusion pressure was calculated using Eq (3).

Through applying the non-linear least squares regression analysis in the Originlab, Basterfield et al. model (Eq (4)) was fitted to the test results. Both the experimental and fitted results are plotted in Fig. 11(b). The correlation between test results and Basterfield et al. model was nearly perfect since the R-squared value of three fitted curves was about 0.99 in all cases. A shear-thinning behavior of all mixtures could be observed from the fitted curves in Fig. 11(b). The rheological parameters, namely, σ_0, k, and n, were determined as well. The shear yield stress of the fresh mixtures was calculated according to Eq (5). Fig. 11(c) reports the obtained shear yield stress and flow consistency. Increasing the HGCC content resulted in increased flow consistency in the fresh mixture. Mixture HCC exhibited the highest shear yield stress. Whereas, there was no apparent difference between mixtures LCC and MCC in shear yield stress.

3.2. *Evaluation of 3D printability*

3.2.1. *Printability window*

In this study, by using 47 mm/s of the printing speed, the printability window of mixtures LCC, MCC, and HCC was noted as 80 min, 70 min, and 30 min, respectively. The printability window of fresh mixtures was reduced by increasing the HGCC substitution (Fig. 12).

3.2.2. *Buildability assessment*

3.2.2.1. *Method 1.* Fig. 13(a) (b) presents the buildability test results by using method 1. In this test, only mixture HCC could be used to stack 21 layers vertically without collapse. Using mixtures LCC and MCC, the printed structure could only maintain its shape until the 10th and 11th layers, respectively. The height of printed structures before the structure was finished or before failure was recorded and plotted in Fig. 13(b). It could be found that the real height of the printed structure is much lower than the theoretical height for all studied mixtures. This is probably due to the cumulative deformation of printed layers and elastic buckling of the printed structure, which is also evident in Fig. 13(a). Increasing the HGCC content could significantly improve the buildability of fresh mixture. As shown in Fig. 13(c), the final collapse was induced by misalignment of the printing path. Two reasons may lead to the instability of printed structures. First, the deformation of the bottom layers gradually increased the nozzle standoff distance, which resulted in the inaccurate layer deposition (This problem could be solved by a real-time height measurement device and a feedback system that was reported by Wolfs et al. [58]. However, this technique was not employed in this study). As shown in Fig. 13(a), the 1st layer of the printed structure was severely compressed. Compared with mixture LCC, the 1st layer of the printed wall showed better shape stability by using mixtures MCC and HCC. Second, since the nozzle could not stop printing immediately after finishing one filament, it was required to remove the excess materials manually. Thus, both sides of each filament displayed uncontrolled shapes and positions in Fig. 13(c). For mixtures LCC and MCC, elastic buckling failure always started from one side to the other of the printed structure (Fig. 13(c)). However, these constraints did not severely influence the printing process of mixture HCC. Through using method 1, the difference in buildability between mixtures MCC and LCC was not clear.

3.2.2.2. *Method 2.* Fig. 14(a) (b) illustrates the maximum stacked-layer number and the corresponding height of the printed structure for different mixtures. The difference between the measured and theoretical heights is much smaller than that of Method 1 (see Figs. 13(b) and 14 (b)). As shown in Figs. 14(a) and 15, the layer thickness is increased

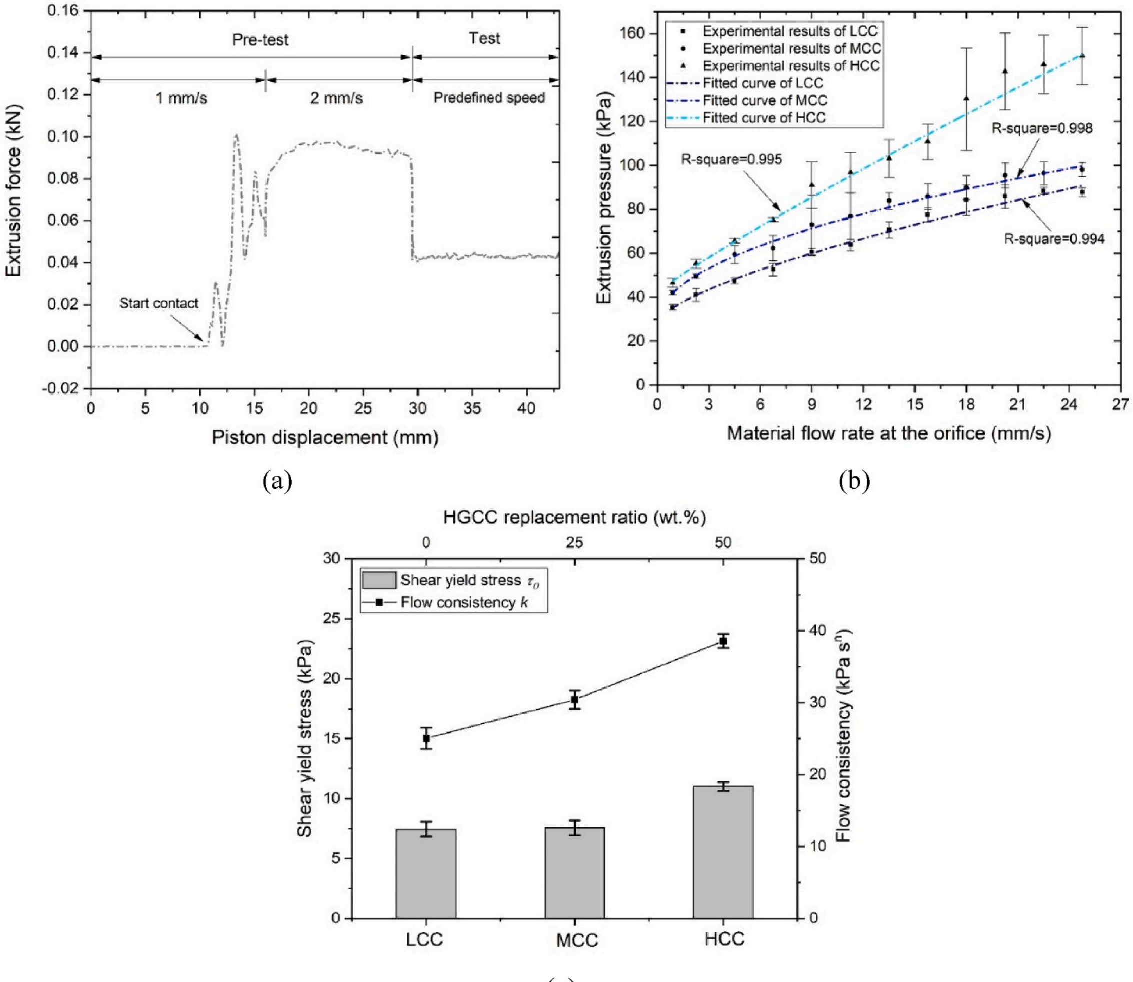

(a)

(b)

(c)

Fig. 11. (a) A typical plot of the ram extrusion test; (b) Experimental results of extrusion pressure with different material flow rates at the orifice and fitted curves via using Basterfield et al. model (Eq (4)); (c) Computed rheological parameters: shear yield stress τ_0, and flow consistency k of mixtures LCC, MCC, and HCC.

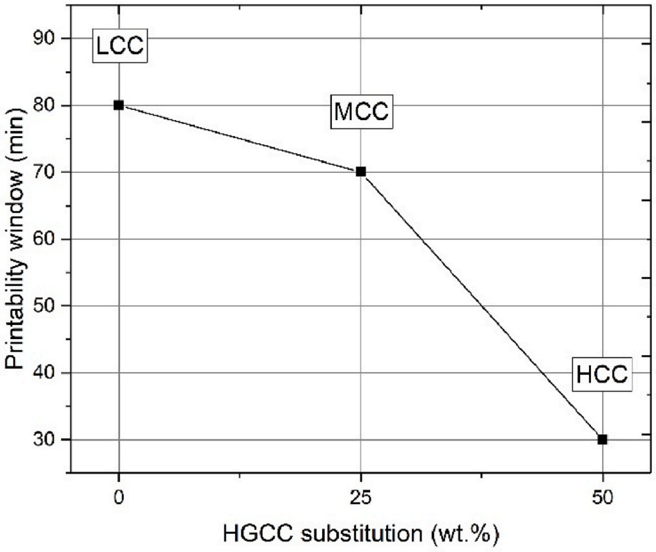

Fig. 12. Printability window various with the HGCC substitution in calcined clay.

from the bottom to the top of the printed structure, especially mixtures LCC and MCC, which may offset the height loss induced by layer deformation. Only mixture HCC could reach the designed layer number without collapse, and showed relatively even layer thickness. In comparison with method 1, the boundary condition of the printed layer in method 2 was more stable. The difference between mixtures LCC and MCC on buildability performance could be indicated.

Overall, the buckling failure of the printed structure may be mainly attributed to the unstable layer deposition, which was induced by the increase of nozzle standoff distance (Figs. 13(c) and 14(c)), and the reduction of layer contacted area (Fig. 15). In method 1, each layer was dropped onto the substrate via a hybrid down- and back-flow nozzle with a rectangle opening (nozzle 1). The contact area between layers was quite stable and constant (Fig. 15). Since a down-flow nozzle with a round opening (nozzle 2) was employed in method 2, the new layer was deposited on the substrate through a squeezed and compressed forming process. The substrate needed to sustain not only the load from the weight of the new layer but also the force from the nozzle. However, this force was not constant during the printing process. It was decreased due to the increase of nozzle standoff distance. The contact area between layers, as well as layer thickness, became more uncontrollable for mixtures with weak buildability as resulting from method 2.

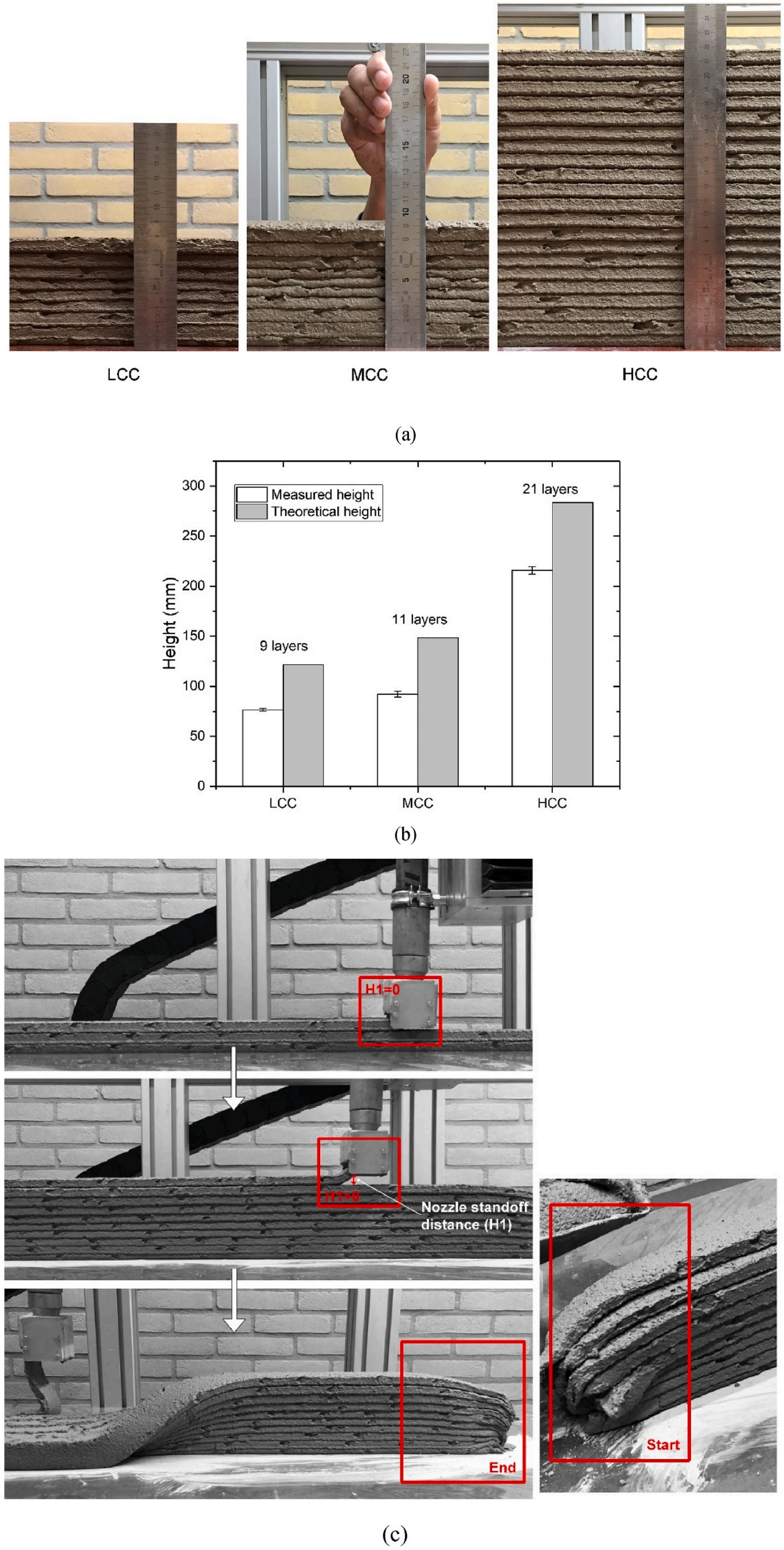

Fig. 13. Buildability test results of method 1: (a) Buildability performance of mixtures LCC, MCC, and HCC; (b) Height and layer number of the printed object by using different mixtures (mixtures LCC and MCC: data recorded before collapse; mixture HCC: data recorded after the 21st layer); (c) Possible reasons for collapse of the rising structure.

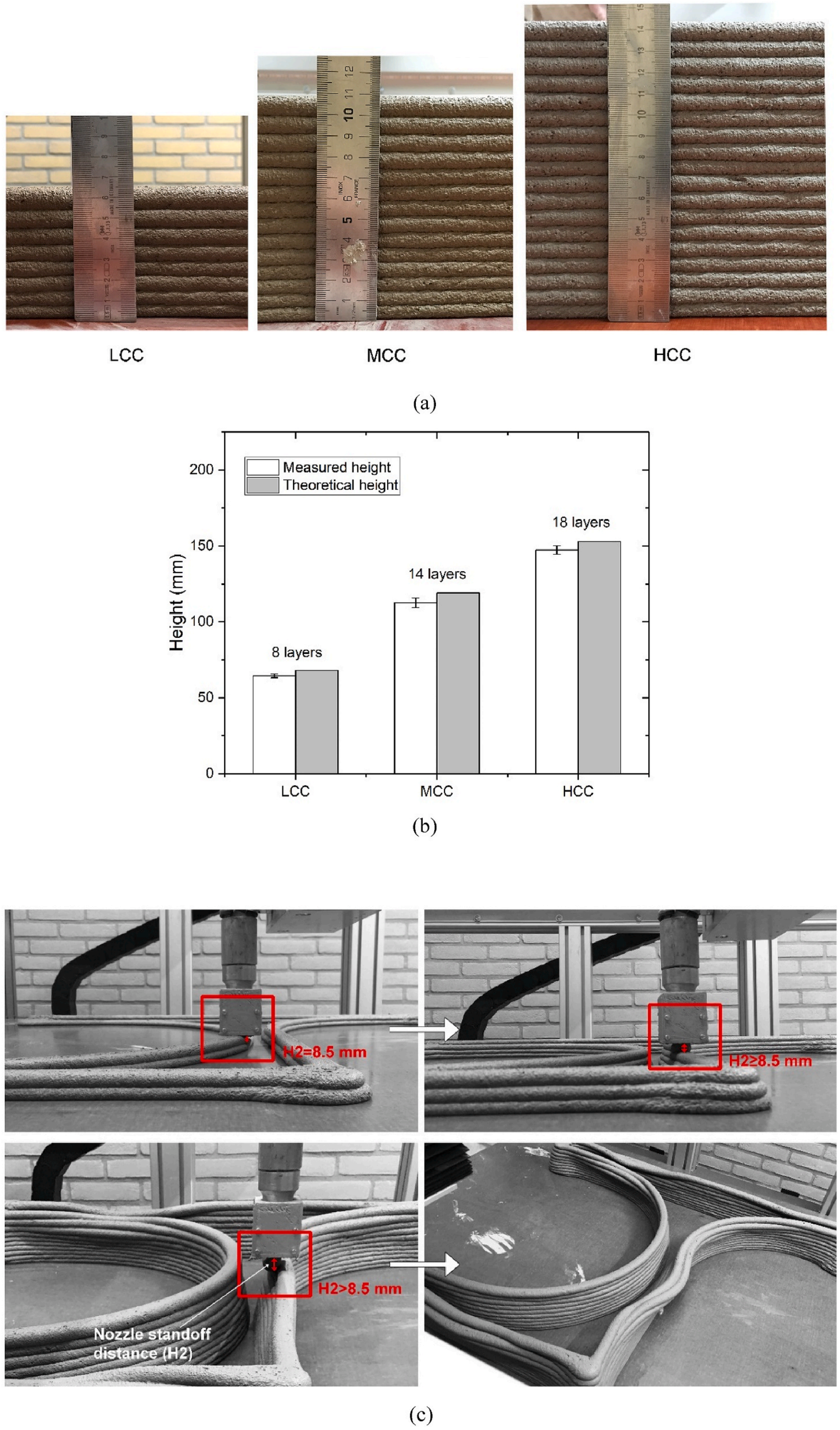

Fig. 14. Buildability test results of method 2: (a) Buildability performance of mixtures LCC, MCC, and HCC; (b) Height and layer number of the printed object by using different mixtures (mixtures LCC and MCC: the maximum height before collapse; mixture HCC: data recorded after the 18th layer); (c) Possible reasons for collapse of the rising structure.

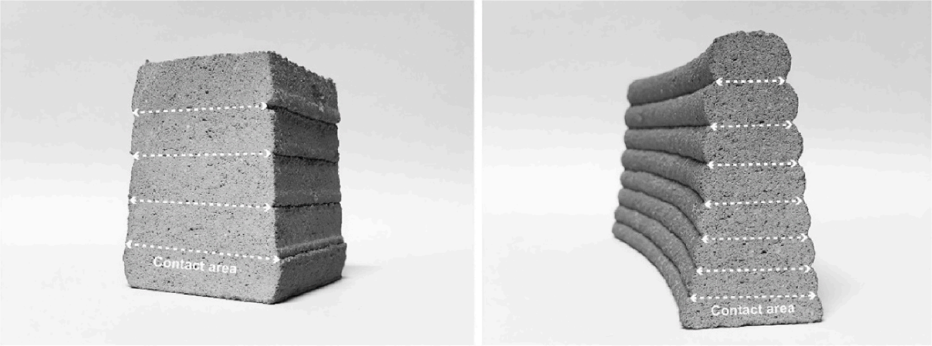

Fig. 15. Cross-sections of printed samples by using nozzle 1 (left) and nozzle 2 (right). The dashed line represents the contact area between two adjacent layers.

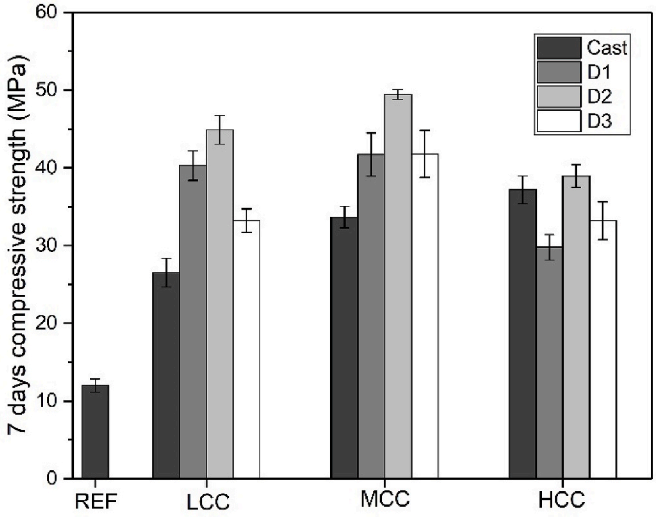

Fig. 16. Compressive strength of both cast and printed samples from different mixtures at the age of 7 days. For test directions D1, D2, and D3, the reader is referred to Fig. 9.

3.3. Compressive strength

Fig. 16 shows the compressive strength of mold-cast and 3D printed samples (except for mixture REF) at 7 days. For cast samples, mixtures containing calcined clay exhibited a much higher compressive strength than mixture REF. Increasing HGCC% in calcined clay improved the compressive strength of cast samples (7 days). The increment of strength between mixtures MCC and HCC was limited. Anisotropic properties were observed for the printed specimens. According to the experimental results, it could be found that the printed specimens displayed the highest compressive strength in loading direction D2 in comparison with directions D1 and D3. The possible reasons have been discussed in Ref. [1,14,59,60]. For mixtures LCC and MCC, the printed samples were stronger than cast samples in all test directions. However, printed samples of mixture HCC had lower compressive strength than its cast samples except for loading direction D2. For printed samples, mixture MCC exhibited the optimal compressive strength at 7 days. In loading directions D1 and D2, mixture LCC showed higher strength than mixture HCC.

3.4. Air void content and distribution

An ROI of 13 mm in height and 25 mm in diameter were obtained in each cylindrical sample. After performing image analysis via ImageJ, the 2D air void content, and the average air void diameter of each slice are computed and plotted in Fig. 17(a) (b). Based on the results of image analysis in Fig. 17(a) (b), for each sample, the interface region could be defined as the region in the height of 5–8 mm due to the relatively higher air void content. The regions of 0–5 mm and 8–13 mm in height could be regarded as the layer area. Fig. 17(a) (b) showed massive air voids with large diameters in the interface region (especially 6–7.5 mm in height) for samples HCC and MCC. Nevertheless, it was relatively difficult to distinguish the interface visually in sample LCC. Compared to samples MCC and HCC, the distribution of air voids in sample LCC was more homogeneous (please also check Appendix A, Figure A.1.). As shown in Fig. 17(c), increasing HGCC% in calcined clay could significantly increase the maximum value of air void content in the interface region. Furthermore, it led to a slight increase in average air void content in both interface and layer regions.

3.5. Hydration kinetics

3.5.1. Isothermal calorimetry

Fig. 18 shows both heat flow and cumulative heat results of all studied mixtures. In Fig. 18 (a), for all curves, the first peak can be attributed to the heat released from the particle wetting, the initial dissolution of the dry components, and the formation of ettringite at an early age [61]. A dormant period was observed, followed by an acceleration period and by the main hydration peak (I). With the absence of calcined clay, mixture REF had the longest dormant time of 12h and took near 38h to reach the main hydration peak, for which the heat flow resulted in the lowest among the studied mixtures. For mixtures LCC, MCC, and HCC, the increase of HGCC content in calcined clay results in, (1) a reduction in the dormant period; (2) a shift of the main hydration peak to the early age; (3) an increase in the intensity of the main hydration peak. Among them, mixture HCC showed the highest chemical reactivity.

After the main hydration peak, a small shoulder (II), which was not present in mixture REF, was observed in the curves of mixtures LCC, MCC, and HCC. According to [14,62–64], peak (II) may be referred to as the aluminate peak. Around 36h after the aluminate peak, a lower but broader peak (III) appeared in the curve of mixtures HCC, MCC, and LCC. The appeared time and intensity of peak (III) were also dependent on the HGCC content in calcined clay. The formation of the AFm phases, which could be attributed to the pozzolanic reaction of MK with the relatively high concentration of CH in the pore solution [39], may be the

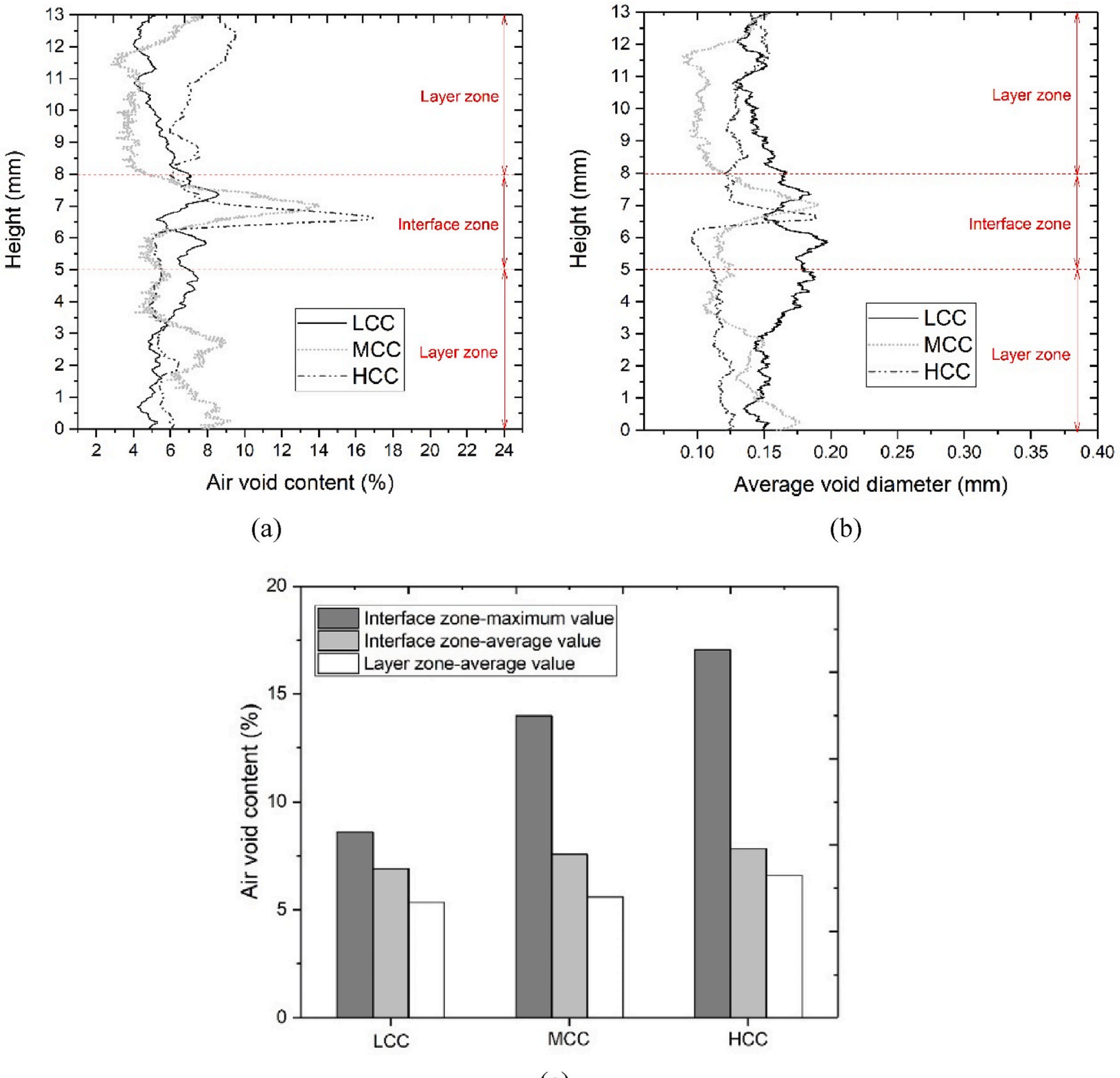

(a) (b)

(c)

Fig. 17. (a) 2D air void content analysis; (b) Average air void diameter analysis; (c) Air void content in the interface and layer zones; Interface zone: 5–8 mm in height of the sample. Layer zone: 0–5 mm and 8–13 mm in height of the sample.

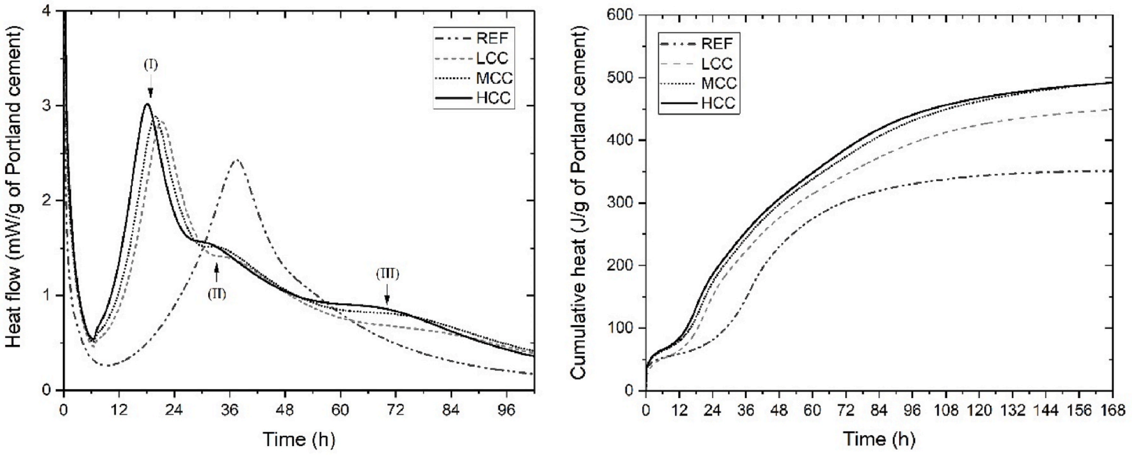

(a) (b)

Fig. 18. Isothermal calorimetry test results of (a) Normalized heat flow with time (4 days). (I)-main hydration peak, (II)-aluminate peak, (III)-AFm/pozzolanic reaction peak; and (b) Normalized cumulative heat with time (7 days).

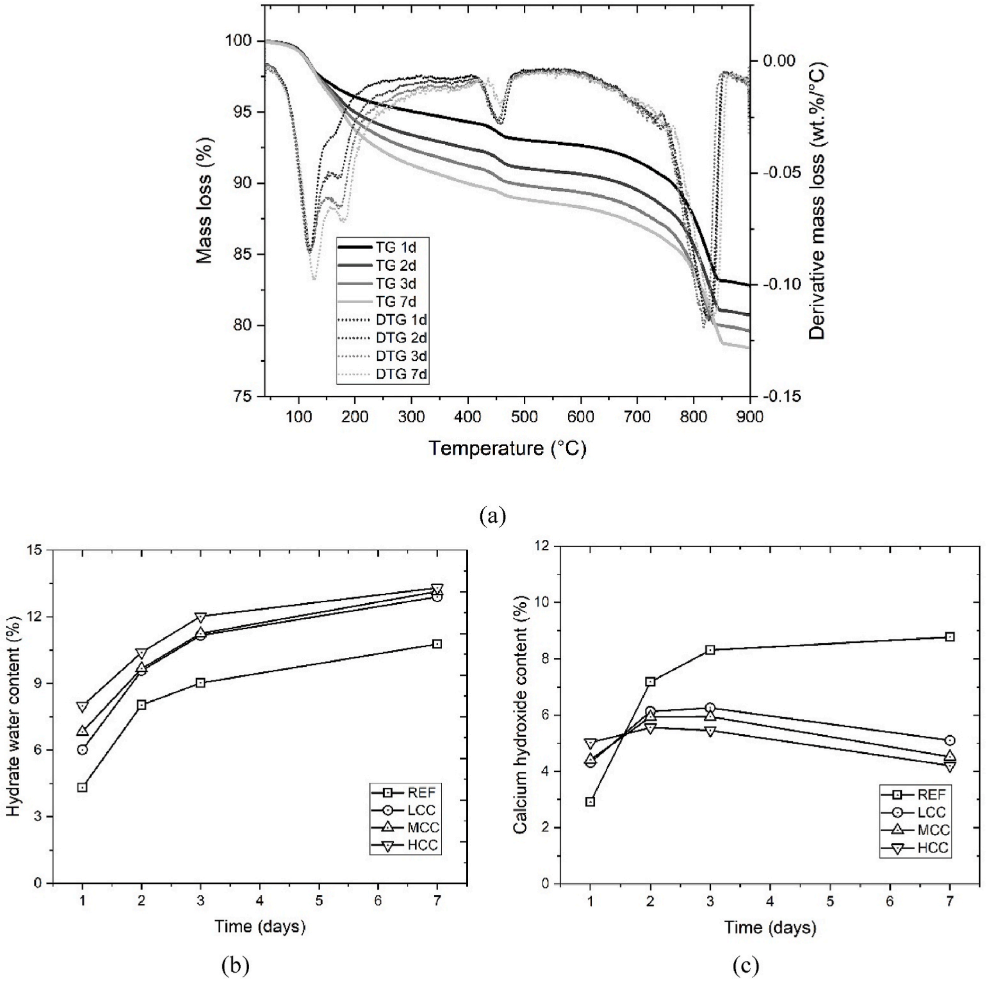

(a)

(b)

(c)

Fig. 19. TGA at 1, 2, 3, and 7 days: (a) a typical example of TG and DTG curves (mixture HCC); (b) The normalized amount of hydrate water (H) relative to the dry sample weight at 600 °C; (c) The normalized amount of calcium hydroxide (CH) relative to the dry sample weight at 600 °C.

Table 7
TG test results-the normalized amount of calcium hydroxide (CH) and hydrate water (H) at 1, 2, 3, and 7 days.

Mixture	Time [days]	H [wt.%]	CH [wt.%]
REF	1	4.31	2.91
	2	8.03	7.18
	3	9.03	8.31
	7	10.77	8.77
LCC	1	6.01	4.31
	2	9.58	6.13
	3	11.16	6.25
	7	12.90	5.10
MCC	1	6.83	4.41
	2	9.67	5.93
	3	11.25	5.94
	7	13.14	4.52
HCC	1	7.99	5.02
	2	10.40	5.56
	3	12.02	5.46
	7	13.30	4.21

reason for the appearance of peak (III). As shown in Fig. 18(b), very low cumulative heat was released in mixture REF, while the addition of calcined clay led to a distinct increase in the cumulative heat of 7 days. For mixtures LCC, MCC, and HCC, it was evident that increasing the dosage of HGCC could significantly increase the total heat emission. Nevertheless, mixtures HCC and MCC showed very close results of the cumulative heat at 7 days.

3.5.2. *Quantification of hydrate water and calcium hydroxide*

Thermogravimetric (TG) curves of different mixtures at 1, 2, 3, and 7 days of curing are illustrated in Fig. 19(a). To identify the boundaries of different phases or groups of phases, derivative thermogravimetric (DTG) curves are plotted in Fig. 19(a) according to TG results. The mass loss during the temperature between 40 °C and 600 °C was regarded as hydrate water (H) [57]. As mentioned by Refs. [57,65], calcium hydroxide (CH) decomposes to calcium oxide and water between 400 °C and 500 °C. For all mixtures in this study, the breakdown of the CH phase ranged between about 420 °C and 500 °C, which can be seen in Fig. 19(a). Peaks above 600 °C are due to the decarbonization of calcite, which is originated from the limestone filler in mixtures and the formed carbonation of CH during the curing time [38]. Therefore, the normalized amount of H and CH were expressed as a percentage of the dry sample weight at 600 °C:

$$W_{[H_2O]} = \frac{M_{40^\circ\mathrm{C}} - M_{600^\circ\mathrm{C}}}{M_{600^\circ\mathrm{C}}} \times 100(\%) \tag{6}$$

and

$$W_{[Ca(OH)_2]} = \frac{M_{420^\circ\mathrm{C}} - M_{500^\circ\mathrm{C}}}{M_{600^\circ\mathrm{C}}} \times \frac{m_{[Ca(OH)_2]}}{m_{H_2O}} \times 100(\%) \tag{7}$$

$W_{[H_2O]}$, and $W_{[Ca(OH)_2]}$ are the mass percentages of H and CH in mixtures, respectively; $M_{40°C}$, $M_{420°C}$, $M_{500°C}$, and $M_{600°C}$ represent the TG results at 40 °C, 420 °C, 500 °C, and 600 °C, respectively; $m_{[Ca(OH)_2]}$, and $m_{[H_2O]}$ stand for the molar masses of CH (74 g/mol) and water (18 g/mol), respectively. The computed results are summarized in Table 7.

The H and CH contents are illustrated in Fig. 19(b) (c). More hydrate water content has been found in mixtures containing calcined clay in comparison with mixture REF within the first 7 days. Replacing part of LGCC by HGCC increased the H amount after 3 days of hydration slightly. At 7 days, mixtures LCC, MCC, and HCC showed similar contents of hydrate water. In comparison with mixture REF, mixtures containing calcined clay showed a much higher amount of CH on the first day of hydration. Increasing HGCC content may contribute to accelerating hydration in the first day. The CH percentage of mixtures LCC, MCC, and HCC kept an increasing trend within the first two days. Afterwards, a significant reduction in the amount of CH was observed until the material age of 7 days. The mixture with a higher HGCC% in calcined clay demonstrated a higher reduction of CH content. Mixture HCC had the lowest CH content already from the second day. However, mixture REF exhibited a much more amount of CH from the second day in contrast to the mixtures containing calcined clay. As mentioned earlier, the consumption of CH could be due to the pozzolanic reaction, which was also indicated as the AFm peak (peak III) in Fig. 18(a). Since this reaction is still under investigation, it was not discussed further in this paper.

4. Discussion

4.1. Effect on 3D printability

In this study, both the average grain size (D_{v50}) and SSA of LGCC are much larger than PC and LP. Partially replacing the content of LP by LGCC resulted in increased SSA_{total} of the mixture (Table 4). HGCC showed a slightly higher SSA than LGCC and much finer grain size when compared to other dry components (LP, PC, and LGCC). According to Ref. [66–68], at a similar water-to-solid ratio, the mean distance between the surface of particles (δ) could be expressed as:

$$\delta = d_{SSA}\left(\left(\frac{\varphi}{\varphi_m}\right)^{-\frac{1}{3}} - 1\right) \tag{8}$$

$$d_{SSA} = \frac{6}{SSA_{total} \times \rho} \tag{9}$$

where d_{SSA} represents the average diameter from the specific surface area, and ρ is the density of the binder mixture. φ and φ_m stand for the solid volume fraction and the maximal packing fraction of solid, respectively. φ_m is not a well-defined parameter that depends on both the spatial distribution of particles and flow history [69]. As suggested in Berodier and Scrivener [66], φ_m can be calculated via the model proposed by Hu and de Larrard [70].

$$\varphi_m = 1 - 0.45\left(\frac{d_{min}}{d_{max}}\right)^{0.19} \tag{10}$$

where $d_{\min}$ and $d_{\max}$ denote the minimum and maximum particle diameters in the mixture. Note that, according to Roussel et al. [67], the obtained result via Eq (10) may overestimate the value of φ_m. As suggested in Ref [66,67,69], φm is assumed as 0.64 for cementitious pastes. Thus, 0.64 was used as the value of φm in the case of the computed value via Eq (10) is larger than 0.64. The effect of admixtures and aggregate on mean interparticle distance was not taken into consideration in this study. Fig. 20(a) indicates that increasing the SSA_{total} could significantly decrease the average interparticle distance.

The partial replacement of LGCC by HGCC in this study did not only change the chemical composition (MK content), but also the physical properties of the binder, i.e., total SSA of solid, and mean interparticle distance (see Fig. 20(a)). Since the ram extrusion test was performed at the material age of 10 min, the physical properties of the powder skeleton may dominate the extrusion rheology of fresh mixture at a constant water-to-binder ratio. An inversely proportional correlation between the mean interparticle distance and flow consistency of the fresh mixture was illustrated in Fig. 20(b). The shear between particles was increased as the interparticle distance diminished [66]. As mentioned by Yahia et al. [71], the increase of interparticle friction induced by the increase of solid to solid contact can be one reason for the increase of viscosity. Fig. 20(b) also shows the relationship between mean particle distance and shear yield stress of fresh mixtures. It seemed that the shear yield stress rarely increased until the mean interparticle distance was smaller than a critical value. To our knowledge, the reason associated with this phenomenon is still not clear.

Regarding the printing quality, the extrusion of fresh mixtures should be performed within the printability window (under a specific printing speed). As reported in Section 3.2.1., the open time under the printing speed of 47 mm/s was reduced by increasing HGCC% in calcined clay. In Section 2.2.2.1., the fresh mixture was not printed continuously during the test, and there was a time interval (5 min) between two subsequent printing sessions. From a microscale view,

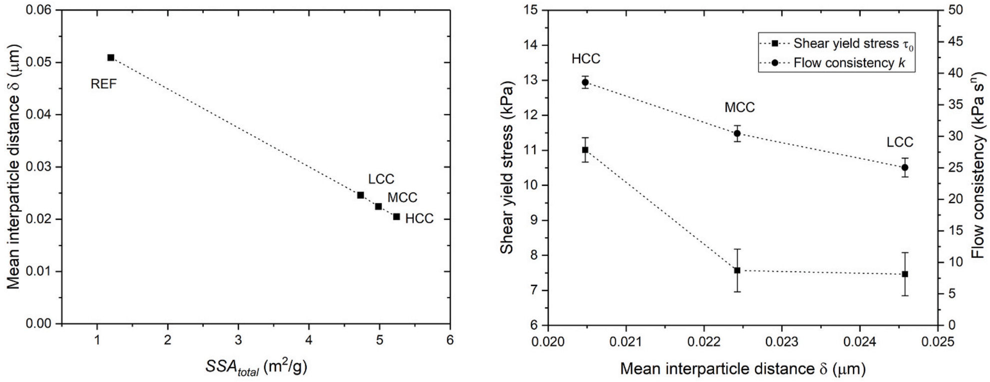

(a) (b)

Fig. 20. Relationship between (a) Mean interparticle distance and total SSA of solid; (b) Mean interparticle distance and shear yield stress as well as flow consistency obtained in Section 3.1.

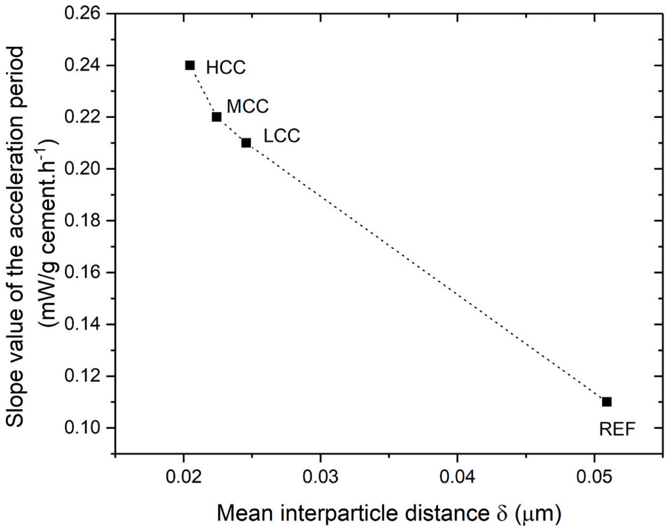

Fig. 21. Slope value of the acceleration period as a function of the mean interparticle distance.

cement particles may experience flocculation, and nucleation during the time interval. Non-reversible hydrate bonds may have been formed between particles, which could still be broken under the effect of sufficient external remixing or shearing force [72,73]. Thus, it is feasible to print the fresh mixture after a short pre-pumping session (5 min) at an earlier age. Nevertheless, the chemical bonds between particles could be rebuilt again at rest [72]. A fixed remixing or shearing force from the printing system seemed insufficient to destroy all the interparticle connections with time passing. Eventually, the significant workability loss led to the termination of the test.

According to Ref. [74,75], the buildability was dominated by the structural build-up behavior of fresh mixture at rest at a series of constant printing parameters (printing speed, time interval, printing setup, and the geometry of the printing path). From a macroscopic observation, increasing the HGCC content in calcined clay could enhance the buildability of fresh mixture, which indicated the increase of structural build-up at rest. Blending HGCC in the mixture may contribute to the enhancement of particle flocculation and increased water adsorption induced by physical characteristics of HGCC particles, i.e., the fine grain size, high specific surface area, and layered structure [43]. However, the obtained results in this study are still insufficient to explain this phenomenon, which is currently under investigation.

4.2. Effect on hydration kinetics

According to the test results in Section 3.5., adding calcined clay in mixtures could significantly accelerate the cement hydration (Fig. 18 (a)), and increase the content of hydration products (CH and H) after the first day (Fig. 19(b) (c)). For mixtures containing calcined clay, 1-day hydration was also accelerated by increasing the HGCC content. As mentioned by Lapeyre and Kumar [76], at a very early age, i.e., within a few hours of hydration, calcined clay (MK) could be regarded as a type of inert filler to provide nucleation sites to increase the hydration rate of clinker. According to our earlier study [44], the increase of MK content reduced the initial setting time significantly. The initial setting time of mixtures REF, LCC, MCC, and HCC are about 260, 150, 80, and 50 min. Thus, the filler effect induced by calcined clay may play the dominant role during the first day of hydration. Increasing HGCC% in calcined clay seemed to promote its filler effect further. Berodier and Scrivener [66] reported that the interparticle distance was the most critical factor in influencing the reaction rate of C_3S hydration. The relationship between the slope of the acceleration period of the main peak and the mean interparticle distance of different binder systems is presented in Fig. 21. The acceleration rate of the main hydration peak was obtained according to Refs. [77,78]. Fig. 21 indicates that the acceleration rate was increased by reducing the average interparticle distance, which agreed with the findings from Ref. [66].

4.3. Effect on compressive strength

The compressive strength at 7 days was measured on both mold-cast and printed samples in Section 3.3. According to the test results from [33,39], increasing the MK content in calcined clay could increase the 7 days compressive strength of LC3-50 system mortar. The test results of cast samples in this paper confirmed these findings. In this study, the only difference for different mixtures is the calcined clay composition. Here we assumed that the air void content and distribution of cast samples were similar among different mixtures. Thus, the compressive strength of cast samples might mainly rely on the hydration of cementitious materials. Positive correlations were obtained between compressive strength of cast samples and normalized cumulative heat (mixtures HCC and MCC showed very close results), as well as the hydrate water content at 7 days in Fig. 22.

However, these correlations could not be formulated for the compressive strength of printed samples. The printed sample of mixture HCC showed the weakest compressive strength at 7 days (see Fig. 16). Generally, for quasi-brittle materials, the increment of porosity could lead to a proportional reduction of strength [79]. Macropores, especially air voids, may dominate the mechanical performance of printed concrete. As shown in Fig. 17, the air void content and distribution of printed samples by using different mixtures were not similar. Chen et al. [80] reported that the maximum value of air void content of the interface region could significantly influence the interlayer bonding strength and anisotropic properties of the printed specimens. In this study, mixture HCC showed the weakest compressive strength, which may be attributed to the highest air void content at the interface (maximum value) of its printed sample.

The possible reasons why the mixtures containing HGCC showed large and more air voids in the interface zone were summarized as follows. First, according to [72,75], for the same time interval and printing environment conditions (ambient temperature and relative humidity), the cold-joint/weaker interface could be easily formed by using a fresh mixture with a high thixotropy/structuration rate. As reported in earlier studies [53,81,82], high amount of air voids between two layers as a

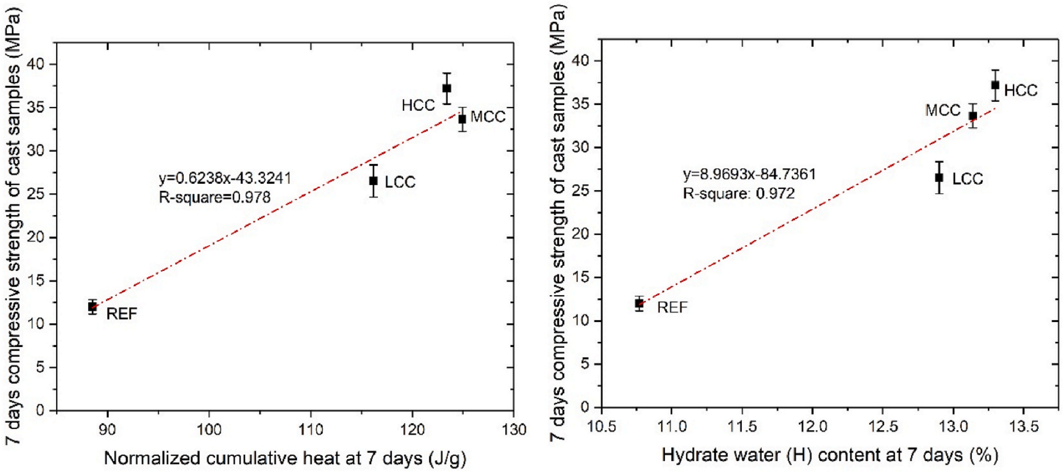

(a) (b)

Fig. 22. The linear relationship between 7 days compressive strength and (a) Normalized cumulative heat at 7 days (excluding any heat within the first 12 h after mixing) obtained from isothermal calorimetry test; (b) Hydrate water (H) content at 7 days obtained from TGA.

typical phenomenon can be found in many 3D printed cementitious materials with a weak interface adhesion. Thus, in this context, the high air void content between layers could be attributed to the high structuration rate of the fresh mixture. Second, in the case of mixtures containing HGCC (mixtures MCC and HCC), after the top layer deposition, the deformation of the substrate was smaller than that of mixture LCC due to the fast growth of material stiffness (as indicated by the high buildability). This may be attributed to the fast particle flocculation and accelerated surface drying process induced by HGCC. Consequently, many unfilled areas were kept forming large air voids between two subsequent layers, as shown in Figure A1.

However, in comparison to mixture LCC, the printed sample of mixture MCC exhibited stronger compressive strength, even containing a higher content of air voids at the interface region (see Fig. 17). Therefore, the compressive strength of printed concrete should rely on both the hydration degree of cementitious materials and the air void content at the interface region.

5. Conclusion

The results yielded from this study indicated the considerable effects of different grades of calcined clay on 3D printability, compressive strength, and hydration of limestone and calcined clay-based cementitious materials. Our findings are summarized as follows:

- For the ram extrusion rheology, an excellent correlation between experimental results and Basterfield et al. model was obtained. Increasing HGCC% in calcined clay could modify not only the MK content, but also the physical property of the fresh mixture, i.e., the increase of total specific surface area, and decrease of mean interparticle distance, which may be the primary reason for the increase of flow consistency of the fresh mixture. A steeper increase of shear yield stress was found between mixtures MCC and HCC, whereas mixture LCC showed a very close value to that of mixture MCC.
- By increasing the HGCC content, the buildability of fresh mixture was noticeably improved, whereas the printability window was reduced. A possible reason was that blending HGCC in the mixture may contribute to the enhancement of particle flocculation and increased water adsorption induced by the fine grain size, high specific surface area, and layered structure of HGCC particles. However, further study is needed to validate this.
- Calcined clay addition (mixtures LCC, MCC, and HCC) resulted in the acceleration of hydration as compared to limestone (mixture REF). The 1-day hydration was enhanced due to the increase in the replacement of HGCC, which may be attributed to the reduction of the mean interparticle distance. A positive correlation between the slope value of the acceleration period and the average interparticle distance was observed.
- For the mold-cast samples, the mixture with higher dosage of HGCC displayed a stronger compressive strength at 7 days, and the hydration degree played a dominant role in the compressive strength development. The obtained results showed a linear relationship between the compressive strength of cast samples and the normalized cumulative heat as well as the hydrate water content at 7 days.
- For the printed samples, the compressive strength at 7 days was not only dependent on the hydration degree but also on the structural build-up of fresh mixtures at rest. The results confirmed that fresh mixtures with good buildability might be vulnerable to enclose more air voids for forming cold joint/weak interface between two adjacent layers. Due to the increase of MK content (HGCC%), more and larger air voids were found in the interface zone, which weakened the compressive strength of printed cementitious materials.

Declaration of competing interest

The authors declare that they have no known competing financial interests or personal relationships that could have appeared to influence the work reported in this paper.

Acknowledgments

Yu Chen, Zhenming Li, and Boyu Chen would like to acknowledge the funding supported by China Scholarship Council under Grant No. 201807720005, 201506120072, and 201708360087, respectively. Claudia Romero Rodriguez acknowledges the financial support from the Construction Technology Research Program funded by the Ministry of Land, Infrastructure and Transport of the Korean Government under the grant 17SCIP-B103706-03. The authors appreciate Mr. Arjan Thijssen, Mr. John van den Berg, Mr. Maiko van Leeuwen and Mr. Koen Jansen for their supports in the experimental tests. Burgess Pigment Company is thanked for the supply of the Optipozz®Burgess metakaolin.

Appendix A

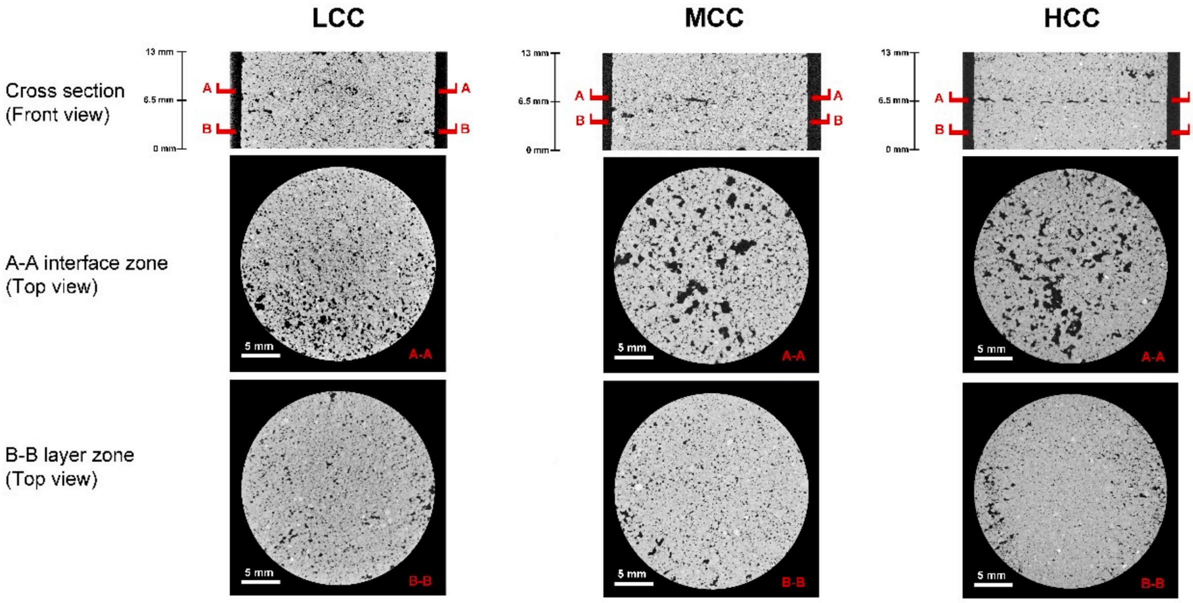

Fig. A.1. Greyscale images of different samples acquired from CT scanning.

References

[1] B. Panda, G.B. Singh, C. Unluer, M.J. Tan, Synthesis and characterization of one-part geopolymers for extrusion based 3D concrete printing, J. Clean. Prod. 220 (2019) 610–619, https://doi.org/10.1016/j.jclepro.2019.02.185.

[2] B. Panda, M.J. Tan, Rheological behavior of high volume fly ash mixtures containing micro silica for digital construction application, Mater. Lett. 237 (2019) 348–351, https://doi.org/10.1016/j.matlet.2018.11.131.

[3] F. Bos, R. Wolfs, Z. Ahmed, T. Salet, Additive manufacturing of concrete in construction: potentials and challenges of 3D concrete printing, Virtual Phys. Prototyp. 11 (2016) 209–225, https://doi.org/10.1080/17452759.2016.1209867.

[4] Y. Chen, S. Chaves Figueiredo, Ç. Yalçinkaya, O. Çopuroğlu, F. Veer, E. Schlangen, The effect of viscosity-modifying admixture on the extrudability of limestone and calcined clay-based cementitious material for extrusion-based 3D concrete printing, Materials 12 (2019) 1374, https://doi.org/10.3390/ma12091374.

[5] V.N. Nerella, M. Näther, A. Iqbal, M. Butler, V. Mechtcherine, Inline quantification of extrudability of cementitious materials for digital construction, Cement Concr. Compos. 95 (2019) 260–270, https://doi.org/10.1016/j.cemconcomp.2018.09.015.

[6] B. Zhu, J. Pan, B. Nematollahi, Z. Zhou, Y. Zhang, J. Sanjayan, Development of 3D printable engineered cementitious composites with ultra-high tensile ductility for digital construction, Mater. Des. 181 (2019) 108088, https://doi.org/10.1016/j.matdes.2019.108088.

[7] L. Reiter, T. Wangler, N. Roussel, R.J. Flatt, The role of early age structural build-up in digital fabrication with concrete, Cement Concr. Res. 112 (2018) 86–95, https://doi.org/10.1016/j.cemconres.2018.05.011.

[8] Y. Chen, F. Veer, O. Çopuroğlu, A critical review of 3D concrete printing as a low CO 2 concrete approach, Heron 62 (2017) 167–194.

[9] Y. Chen, F. Veer, O. Copuroglu, E. Schlangen, Feasibility of using low CO2 concrete alternatives in extrusion-based 3D concrete printing, in: T. Wangler, R. Flatt (Eds.), First RILEM Int. Conf. Concr. Digit. Fabr. – Digit. Concr, Springer, Cham, 2019, pp. 269–276, https://doi.org/10.1007/978-3-319-99519-9_25.

[10] G. Ma, Y. Li, L. Wang, J. Zhang, Z. Li, Real-time quantification of fresh and hardened mechanical property for 3D printing material by intellectualization with piezoelectric transducers, Construct. Build. Mater. 241 (2020) 117982, https://doi.org/10.1016/j.conbuildmat.2019.117982.

[11] R.A. Buswell, W.R. Leal de Silva, S.Z. Jones, J. Dirrenberger, 3D printing using concrete extrusion: a roadmap for research, Cement Concr. Res. 112 (2018) 37–49, https://doi.org/10.1016/j.cemconres.2018.05.006.

[12] V.N. Nerella, M. Krause, V. Mechtcherine, Direct printing test for buildability of 3D-printable concrete considering economic viability, Autom. ConStruct. 109 (2020) 102986, https://doi.org/10.1016/j.autcon.2019.102986.

[13] B. Panda, S. Ruan, C. Unluer, M.J. Tan, Improving the 3D printability of high volume fly ash mixtures via the use of nano attapulgite clay, Compos. B Eng. 165 (2019) 75–83, https://doi.org/10.1016/j.compositesb.2018.11.109.

[14] Y. Chen, S. Chaves Figueiredo, Z. Li, Z. Chang, K. Jansen, O. Çopuroğlu, E. Schlangen, Improving printability of limestone-calcined clay-based cementitious materials by using viscosity-modifying admixture, Cement Concr. Res. 132 (2020) 106040, https://doi.org/10.1016/j.cemconres.2020.106040.

[15] B. Panda, C. Unluer, M.J. Tan, Investigation of the rheology and strength of geopolymer mixtures for extrusion-based 3D printing, Cement Concr. Compos. 94 (2018) 307–314, https://doi.org/10.1016/j.cemconcomp.2018.10.002.

[16] A. Kazemian, X. Yuan, E. Cochran, B. Khoshnevis, Cementitious materials for construction-scale 3D printing: laboratory testing of fresh printing mixture, Construct. Build. Mater. 145 (2017) 639–647, https://doi.org/10.1016/j.conbuildmat.2017.04.015.

[17] E. Hosseini, M. Zakertabrizi, A.H. Korayem, G. Xu, A novel method to enhance the interlayer bonding of 3D printing concrete: an experimental and computational investigation, Cement Concr. Compos. 99 (2019) 112–119, https://doi.org/10.1016/j.cemconcomp.2019.03.008.

[18] S.C. Paul, G.P.A.G. van Zijl, M.J. Tan, I. Gibson, A review of 3D concrete printing systems and materials properties: current status and future research prospects, Rapid Prototyp. J. 24 (2018), https://doi.org/10.1108/RPJ-09-2016-0154, 00–00.

[19] S.C. Paul, Y.W.D. Tay, B. Panda, M.J. Tan, Fresh and hardened properties of 3D printable cementitious materials for building and construction, Arch. Civ. Mech. Eng. 18 (2018) 311–319, https://doi.org/10.1016/j.acme.2017.02.008.

[20] Y. Weng, M. Li, M.J. Tan, S. Qian, Design 3D printing cementitious materials via Fuller Thompson theory and Marson-Percy model, Construct. Build. Mater. 163 (2018) 600–610, https://doi.org/10.1016/j.conbuildmat.2017.12.112.

[21] Z. Liu, M. Li, Y. Weng, T.N. Wong, M.J. Tan, Mixture Design Approach to optimize the rheological properties of the material used in 3D cementitious material printing, Construct. Build. Mater. 198 (2019) 245–255, https://doi.org/10.1016/j.conbuildmat.2018.11.252.

[22] X. Zhou, Z. Li, Characterization of rheology of fresh fiber reinforced cementitious composites through ram extrusion, Mater. Struct. Constr. 38 (2005) 17–24, https://doi.org/10.1617/14064.

[23] S. Chaves Figueiredo, C. Romero Rodríguez, Z.Y. Ahmed, D.H. Bos, Y. Xu, T. M. Salet, O. Çopuroğlu, E. Schlangen, F.P. Bos, An approach to develop printable strain hardening cementitious composites, Mater. Des. 169 (2019), https://doi.org/10.1016/j.matdes.2019.107651.

[24] A. Perrot, D. Rangeard, V. Nerella, V. Mechtcherine, Extrusion of cement-based materials - an overview, RILEM Tech. Lett. 3 (2019) 91–97, https://doi.org/10.21809/rilemtechlett.2018.75.

[25] A. Perrot, Y. Mélinge, D. Rangeard, F. Micaelli, P. Estellé, C. Lanos, Use of ram extruder as a combined rheo-tribometer to study the behaviour of high yield stress fluids at low strain rate, Rheol. Acta 51 (2012) 743–754, https://doi.org/10.1007/s00397-012-0638-6.

[26] X. Zhou, Z. Li, M. Fan, H. Chen, Rheology of semi-solid fresh cement pastes and mortars in orifice extrusion, Cement Concr. Compos. 37 (2013) 304–311, https://doi.org/10.1016/j.cemconcomp.2013.01.004.

[27] R.A. Basterfield, C.J. Lawrence, M.J. Adams, On the interpretation of orifice extrusion data for viscoplastic materials, Chem. Eng. Sci. 60 (2005) 2599–2607, https://doi.org/10.1016/j.ces.2004.12.019.

[28] T.T. Le, S.A. Austin, S. Lim, R.A. Buswell, A.G.F. Gibb, T. Thorpe, Mix design and fresh properties for high-performance printing concrete, Mater. Struct. Constr. 45 (2012) 1221–1232, https://doi.org/10.1617/s11527-012-9828-z.

[29] G. Ma, Z. Li, L. Wang, Printable properties of cementitious material containing copper tailings for extrusion based 3D printing, Construct. Build. Mater. 162 (2018) 613–627, https://doi.org/10.1016/j.conbuildmat.2017.12.051.

[30] A.V. Rahul, M. Santhanam, H. Meena, Z. Ghani, 3D printable concrete: mixture design and test methods, Cement Concr. Compos. 97 (2019) 13–23, https://doi.org/10.1016/j.cemconcomp.2018.12.014.

[31] G. Ma, J. Sun, L. Wang, F. Aslani, M. Liu, Electromagnetic and microwave absorbing properties of cementitious composite for 3D printing containing waste copper solids, Cement Concr. Compos. 94 (2018) 215–225, https://doi.org/10.1016/j.cemconcomp.2018.09.005.

[32] K. Scrivener, F. Martirena, S. Bishnoi, S. Maity, Calcined clay limestone cements (LC3), Cement Concr. Res. 114 (2018) 49–56, https://doi.org/10.1016/j.cemconres.2017.08.017.

[33] F. Avet, R. Snellings, A. Alujas Diaz, M. Ben Haha, K. Scrivener, Development of a new rapid, relevant and reliable (R3) test method to evaluate the pozzolanic reactivity of calcined kaolinitic clays, Cement Concr. Res. 85 (2016) 1–11, https://doi.org/10.1016/j.cemconres.2016.02.015.

[34] W. Huang, H. Kazemi-Kamyab, W. Sun, K. Scrivener, Effect of replacement of silica fume with calcined clay on the hydration and microstructural development of eco-UHPFRC, Mater. Des. 121 (2017) 36–46, https://doi.org/10.1016/j.matdes.2017.02.052.

[35] Y. Dhandapani, M. Santhanam, Assessment of pore structure evolution in the limestone calcined clay cementitious system and its implications for performance, Cement Concr. Compos. 84 (2017) 36–47, https://doi.org/10.1016/j.cemconcomp.2017.08.012.

[36] A. Tironi, A.N. Scian, E.F. Irassar, Blended cements with limestone filler and kaolinitic calcined clay: filler and pozzolanic effects, J. Mater. Civ. Eng. 29 (2017), 04017116, https://doi.org/10.1061/(asce)mt.1943-5533.0001965.

[37] G.L. Alvarez, A. Nazari, A. Bagheri, J.G. Sanjayan, C. De Lange, Microstructure, electrical and mechanical properties of steel fibres reinforced cement mortars with partial metakaolin and limestone addition, Construct. Build. Mater. 135 (2017) 8–20, https://doi.org/10.1016/j.conbuildmat.2016.12.170.

[38] M. Antoni, J. Rossen, F. Martirena, K. Scrivener, Cement substitution by a combination of metakaolin and limestone, Cement Concr. Res. 42 (2012) 1579–1589, https://doi.org/10.1016/j.cemconres.2012.09.006.

[39] F. Avet, K. Scrivener, Investigation of the calcined kaolinite content on the hydration of limestone calcined clay cement (LC3), Cement Concr. Res. 107 (2018) 124–135, https://doi.org/10.1016/j.cemconres.2018.02.016.

[40] R. San Nicolas, M. Cyr, G. Escadeillas, Characteristics and applications of flash metakaolins, Appl. Clay Sci. 83–84 (2013) 253–262, https://doi.org/10.1016/j.clay.2013.08.036.

[41] D. Zhao, R. Khoshnazar, Microstructure of cement paste incorporating high volume of low-grade metakaolin, Cement Concr. Compos. 106 (2020) 103453, https://doi.org/10.1016/j.cemconcomp.2019.103453.

[42] N.A. Tregger, M.E. Pakula, S.P. Shah, Influence of clays on the rheology of cement pastes, Cement Concr. Res. 40 (2010) 384–391, https://doi.org/10.1016/j.cemconres.2009.11.001.

[43] T.R. Muzenda, P. Hou, S. Kawashima, T. Sui, X. Cheng, The role of limestone and calcined clay on the rheological properties of LC3, Cement Concr. Compos. 107 (2020) 103516, https://doi.org/10.1016/j.cemconcomp.2020.103516.

[44] Y. Chen, Z. Li, S.C. Figueiredo, O. Copuroglu, F. Veer, E. Schlangen, Limestone and calcined clay-based sustainable cementitious materials for 3D concrete printing: a fundamental study of extrudability and early-age strength development, Appl. Sci. 9 (2019), https://doi.org/10.3390/app9091809.

[45] S. Ferreiro, M.M.C. Canut, J. Lund, D. Herfort, Influence of fineness of raw clay and calcination temperature on the performance of calcined clay-limestone blended cements, Appl. Clay Sci. 169 (2019) 81–90, https://doi.org/10.1016/j.clay.2018.12.021.

[46] S. Ferreiro, D. Herfort, J.S. Damtoft, Effect of raw clay type, fineness, water-to-cement ratio and fly ash addition on workability and strength performance of calcined clay – limestone Portland cements, Cement Concr. Res. 101 (2017) 1–12, https://doi.org/10.1016/j.cemconres.2017.08.003.

[47] J. Skibsted, R. Snellings, Reactivity of supplementary cementitious materials (SCMs) in cement blends, Cement Concr. Res. 124 (2019), https://doi.org/10.1016/j.cemconres.2019.105799.

[48] M.A.B. Beigh, V.N. Nerella, C. Schröfl, V. Mechtcherine, Studying the rheological behavior of limestone calcined clay cement (LC^3) mixtures in the context of extrusion-based 3D-printing, in: 3rd Int. Conf. Calcined Clays Sustain. Concr., Delhi, 2019, pp. 1–8. https://www.researchgate.net/publication/336616922_Studying_the_rheological_behavior_of_limestone_calcined_clay_cement_LC_mixtures_in_the_context_of_extrusion-_based_3D-printing.

[49] C. Aramburo, C. Pedrajas, V. Rahhal, M. González, R. Talero, Calcined clays for low carbon cement: rheological behaviour in fresh Portland cement pastes, Mater. Lett. 239 (2019) 24–28, https://doi.org/10.1016/j.matlet.2018.12.050.

[50] NEN-EN 196-2, Method of Testing Cement - Part 2: Chemical Analysis of Cement, 2013.

[51] T. Matschei, B. Lothenbach, F.P. Glasser, The role of calcium carbonate in cement hydration, Cement Concr. Res. 37 (2007) 551–558, https://doi.org/10.1016/j.cemconres.2006.10.013.

[52] R.J.M. Wolfs, F.P. Bos, T.A.M. Salet, Hardened properties of 3D printed concrete: the influence of process parameters on interlayer adhesion, Cement Concr. Res. 119 (2019) 132–140, https://doi.org/10.1016/j.cemconres.2019.02.017.

[53] V.N. Nerella, S. Hempel, V. Mechtcherine, Effects of layer-interface properties on mechanical performance of concrete elements produced by extrusion-based 3D-printing, Construct. Build. Mater. 205 (2019) 586–601, https://doi.org/10.1016/j.conbuildmat.2019.01.235.

[54] NEN-EN 196-1, Methods of Testing Cement - Part 1: Determination of Strength, 2016.

[55] O. Çopuroğlu, Revealing the dark side of portlandite clusters in cement paste by circular polarization microscopy, Materials 9 (2016), https://doi.org/10.3390/ma9030176.

[56] S. Chaves Figueiredo, O. Çopuroğlu, E. Schlangen, Effect of viscosity modifier admixture on Portland cement paste hydration and microstructure, Construct. Build. Mater. 212 (2019) 818–840, https://doi.org/10.1016/j.conbuildmat.2019.04.020.

[57] B. Lothenbach, P. Durdzinski, K. De Weerdt, Thermogravimetric analysis, in: K. Scrivener, R. Snellings, B. Lothenbach (Eds.), A Pract. Guid. To Microstruct. Anal. Cem. Mater., CRC press, 2016, pp. 177–212.

[58] R.J.M. Wolfs, F.P. Bos, E.C.F. van Strien, T.A.M. Salet, A real-time height measurement and feedback system for 3D concrete printing, in: D.A. Hordijk, M. Luković (Eds.), High Tech Concr. Where Technol. Eng. Meet - Proc. 2017 Fib Symp., Maastricht, 2017, https://doi.org/10.1007/978-3-319-59471-2.

[59] T.T. Le, S.A. Austin, S. Lim, R.A. Buswell, R. Law, A.G.F. Gibb, T. Thorpe, Hardened properties of high-performance printing concrete, Cement Concr. Res. 42 (2012) 558–566, https://doi.org/10.1016/j.cemconres.2011.12.003.

[60] B. Panda, S.C. Paul, L.J. Hui, Y.W.D. Tay, M.J. Tan, Additive manufacturing of geopolymer for sustainable built environment, J. Clean. Prod. 167 (2017) 281–288, https://doi.org/10.1016/j.jclepro.2017.08.165.

[61] P.S. de Silva, F.P. Glasser, Hydration of cements based on metakaolin: Thermochemistry, Adv. Cement Res. 3 (1990) 167–177, https://doi.org/10.1680/adcr.1990.3.12.167.

[62] F. Zunino, K. Scrivener, The influence of the filler effect on the sulfate requirement of blended cements, Cement Concr. Res. 126 (2019) 105918, https://doi.org/10.1016/j.cemconres.2019.105918.

[63] J.W. Bullard, H.M. Jennings, R.A. Livingston, A. Nonat, G.W. Scherer, J. S. Schweitzer, K.L. Scrivener, J.J. Thomas, Mechanisms of cement hydration, Cement Concr. Res. 41 (2011) 1208–1223, https://doi.org/10.1016/j.cemconres.2010.09.011.

[64] D. Jansen, F. Goetz-Neunhoeffer, B. Lothenbach, J. Neubauer, The early hydration of Ordinary Portland Cement (OPC): an approach comparing measured heat flow with calculated heat flow from QXRD, Cement Concr. Res. 42 (2012) 134–138, https://doi.org/10.1016/j.cemconres.2011.09.001.

[65] R. Roychand, S. De Silva, D. Law, S. Setunge, High volume fly ash cement composite modified with nano silica, hydrated lime and set accelerator, Mater. Struct. Constr. 49 (2016) 1997–2008, https://doi.org/10.1617/s11527-015-0629-z.

[66] E. Berodier, K. Scrivener, Understanding the filler effect on the nucleation and growth of C-S-H, J. Am. Ceram. Soc. 97 (2014) 3764–3773, https://doi.org/10.1111/jace.13177.

[67] N. Roussel, A. Lemaître, R.J. Flatt, P. Coussot, Steady state flow of cement suspensions: a micromechanical state of the art, Cement Concr. Res. 40 (2010) 77–84, https://doi.org/10.1016/j.cemconres.2009.08.026.

[68] F. De Larrard, Concrete Mixture Proportioning: A Scientific Approach, CRC Press, London, 2005, https://doi.org/10.1017/CBO9781107415324.004.

[69] P. Coussot, Introduction to the Rheology of Complex Fluids, Woodhead Publishing, 2011, https://doi.org/10.1016/B978-0-85709-028-7.50001-7.

[70] C. Hu, F. de Larrard, The rheology of fresh high-performance concrete, Cement Concr. Res. 26 (1996) 283–294, https://doi.org/10.1016/0008-8846(95)00213-8.

[71] A. Yahia, M. Tanimura, Y. Shimoyama, Rheological properties of highly flowable mortar containing limestone filler-effect of powder content and W/C ratio, Cement Concr. Res. 35 (2005) 532–539, https://doi.org/10.1016/j.cemconres.2004.05.008.

[72] N. Roussel, Rheological requirements for printable concretes, Cement Concr. Res. 112 (2018) 76–85, https://doi.org/10.1016/j.cemconres.2018.04.005.

[73] N. Roussel, G. Ovarlez, S. Garrault, C. Brumaud, The origins of thixotropy of fresh cement pastes, Cement Concr. Res. 42 (2012) 148–157, https://doi.org/10.1016/j.cemconres.2011.09.004.

[74] A. Perrot, D. Rangeard, A. Pierre, Structural built-up of cement-based materials used for 3D-printing extrusion techniques, Mater. Struct. 49 (2016) 1213–1220, https://doi.org/10.1617/s11527-015-0571-0.

[75] T. Wangler, E. Lloret, L. Reiter, N. Hack, F. Gramazio, M. Kohler, M. Bernhard, B. Dillenburger, J. Buchli, N. Roussel, R. Flatt, Digital concrete: opportunities and challenges, RILEM Tech. Lett. 1 (2016) 67, https://doi.org/10.21809/rilemtechlett.2016.16.

[76] J. Lapeyre, A. Kumar, Influence of pozzolanic additives on hydration mechanisms of tricalcium silicate, J. Am. Ceram. Soc. 101 (2018) 3557–3574, https://doi.org/10.1111/jace.15518.

[77] E. Berodier, Impact of the Supplementary Cementitious Materials on the Kinetics and Microstructural Development of Cement Hydration, EPFL, 2015, https://doi.org/10.5075/EPFL-THESIS-6417.

[78] M.M. Costoya Fernandez, Effect of Particle Size on the Hydration Kinetics and Microstructural Development of Tricalcium Silicate, EPFL, 2008, https://doi.org/10.5075/epfl-thesis-4102.

[79] D. Liu, B. Šavija, G.E. Smith, P.E.J. Flewitt, T. Lowe, E. Schlangen, Towards understanding the influence of porosity on mechanical and fracture behaviour of quasi-brittle materials: experiments and modelling, Int. J. Fract. 205 (2017) 57–72, https://doi.org/10.1007/s10704-017-0181-7.

[80] Y. Chen, K. Jansen, H. Zhang, C. Romero Rodriguez, Y. Gan, O. Copuroglu, E. Schlangen, Effect of printing parameters on interlayer bond strength of 3D printed limestone calcined clay-based cementitious material: An experimental and numerical study, Constr. Build. Mater. 262 (2020), https://doi.org/10.1016/j.conbuildmat.2020.120094.

[81] Y.W.D. Tay, G.H.A. Ting, Y. Qian, B. Panda, L. He, M.J. Tan, Time gap effect on bond strength of 3D-printed concrete, Virtual Phys. Prototyp. 14 (2019) 104–113, https://doi.org/10.1080/17452759.2018.1500420.

[82] E. Keita, H. Bessaies-Bey, W. Zuo, P. Belin, N. Roussel, Weak bond strength between successive layers in extrusion-based additive manufacturing: measurement and physical origin, Cement Concr. Res. 123 (2019) 105787, https://doi.org/10.1016/j.cemconres.2019.105787.